An Insight into the Interaction between α-Ketoamide-based Inhibitor and Coronavirus Main Protease: A Detailed *in silico* Study

Snehasis Banerjee*[1],

[1]*Department of Chemistry, Government College of Engineering and Leather Technology, Salt Lake, Sector-3, Kolkata, PIN-700106, West Bengal, India*

KEYWORDS: Coronavirus, SARS-CoV, SARS-CoV-2, Covid-19, α-ketoamide, reaction mechanism, cysteine protease, non-covalent interaction, ONIOM

ABSTRACT: The search for therapeutic drugs that can neutralize the effects of COVID-2019 (SARS-CoV-2) infection is the main focus of current research. The coronavirus main protease (M_{pro}) is an attractive target for anti-coronavirus drug design. Further, α-ketoamide is proved to be very effective as a reversible covalent-inhibitor against cysteine proteases. Herein, we report on the non-covalent to the covalent adduct formation mechanism of α-ketoamide-based inhibitor with the enzyme active site amino acids by QM/SQM model (QM= quantum mechanical, SQM= semi-empirical QM). To uncover the mechanism, we focused on two approaches: a concerted and a stepwise fashion. The concerted pathway proceeds *via* deprotonation of the thiol of cysteine (here, Cys_{145} SγH) and simultaneous reversible nucleophilic attack of sulfur onto the α-ketoamide warhead. In this work, we propose three plausible concerted pathways. On the contrary, in a traditional two-stage pathway, the first step is proton transfer from Cys_{145} SγH to His_{41} Nδ forming an ion pair, and consecutively, in the second step, the thiolate ion attacks the α-keto group to form a thiohemiketal. In this reaction, we find that the stability of the tetrahedral intermediate oxyanion/hydroxyl hole plays an important role. Moreover, as the α-keto group

has two faces *Si* or *Re* for the nucleophilic attack, we considered both possibilities of attack leading to S– and R–thiohemiketal. We computed the structural, electronic, and energetic parameters of all stationary points including transition states *via* ONIOM methodology at B3LYP/6-31G(d):PM6 level. Furthermore, to get more accurate results, we also calculated the single-point dispersion-corrected energy profile by using ωB97X-D/6-31G(d,p):PM6 level. Additionally, to characterize covalent, weak noncovalent interaction (NCI) and hydrogen-bonds, we applied NCI-reduced density gradient (NCI-RDG) methods along with Bader's Quantum Theory of Atoms-in-Molecules (QTAIM) and natural bonding orbital (NBO) analysis.

1. INTRODUCTION

A new human coronavirus (HCoV), SARS-CoV-2, began spreading in December 2019 in Wuhan City, China causing pneumonia called COVID-19. All the affected countries are trying to prevent the spread of the new mysterious coronavirus. Despite this, the number of infected persons is continually increasing each day. As the viral maturation mainly relies on the M_{pro}'s activity, the coronavirus main protease (M_{pro}) (also called 3C like protease or $3CL_{pro}$) is also an attractive target for anti-CoV drug design. Recently, it is reported that deadlier coronavirus is highly similar with 96% sequence identity to that of the SARS-CoV M_{pro}.[1] Due to this worldwide pandemic, considerable research is focused to design many inhibitors for the novel coronavirus.[2-10] For drug designing, the reversible covalent inhibitors are generally more preferable than irreversible ones due to its risks in long term treatment and side effects.[11-14] In addition to the development of novel drugs, researchers look for effective substances among drugs that are already approved or developed for other purposes.

Covalent inhibitors, that bind with cysteine proteases, are generally substrate with an electrophilic center, including Michael acceptor (–CH=CH–CO–), aldehydes (–CH=O), nitriles (–C≡N), vinyl sulfone ($–SO_2–CH=CH_2$), and α-ketoamide (–CO–CO–NH–).[15-22] Of them, α-ketoamide proved to be very effective against cysteine proteases.[23] The advantage of the α-ketoamides is that their warhead can interact with the catalytic center of the target proteases by two hydrogen-bonding interactions, namely, *via* the

α-keto oxygen and amide oxygen.[1] Whereas, warheads like aldehydes or Michael acceptors interacts with the catalytic center by only one hydrogen bond, the α-ketoamide motif is emerging as the most promising group with a possible reversible inhibition of the enzyme's activity better than the other investigated C-terminus warheads[23,24] The α-keto group of the α-ketoamide forms a reversible tetrahedral adduct with the active cysteine enzyme. For example, calpain I inhibitors form tetrahedral hemiketal adduct by the cysteine residue (Cys_{115}) onto the α-keto group of the α-ketoamide.[25] Chen J-C *et al.*[26] synthesized a series of small molecules bearing an α-ketoamide warhead and evaluated for their ability to inhibit cathepsin S. In another study, Ota. E. *et. al.*[27] showed that thienyl-Substituted α-ketoamide is a less hydrophobic reactive group for photo-affinity labeling. Recently, Hilgenfeld and his coworkers,[1,28] designed a series of α-ketoamide as inhibitors of SARS-CoV-2 M_{pro}.

Whereas, few theoretical studies about the reaction mechanism of a cysteine protease with Michael acceptor, aldehydes, and nitriles and similar researches are present in literature[29-39] but precise reaction mechanism of α-ketoamide and cysteine is rarely reported.[40] It is essential to understand the inhibitory action of these drugs to design a more promising drug against coronavirus. Commonly, it is believed that in these mechanisms, the first step is deprotonation of thiol of cysteine with a basic side chain, usually by a histidine residue followed by a nucleophilic attack of the anionic sulfur onto the α-keto group of the inhibitor forming an S–C covalent bond and an oxyanion hole. In the last step, the oxyanion gets stability by hydrogen bonds and/or by accepting a proton. To date, few studies have been made to understand how the keto group binds with the cysteine proteases. In particular, to the best of our knowledge, the literature lacks the detailed quantum chemical study of α-ketoamide based inhibitors.

In the present paper, for the first time, we will investigate the detailed reaction mechanism for the conversion of noncovalent adduct to covalent adduct by the interaction of Mpro of coronavirus and two α-ketoamide compounds with the help of semi-empirical and density functional (DFT) studies. We extracted these compounds from the pdb file 6y2f and 5n19 (henceforth, we name them as S-In and R-

In). We considered two approaches for the reaction: i) a concerted and ii) a stepwise mechanism. In the first case, the nucleophilic attack and such proton transfer occur in a single step. Herein, we considered four pathways, for example, Pathways 1−3, as shown in Scheme 1. On the other hand, the second case involves a two-step process (Pathway 4). In the first step, a zwitterionic ion pair ($CysS^{-}/HisN^{+}$) is formed from the fast proton transfer from cysteine (Cys_{145}) to nearby histidine residue (His_{41}) (Scheme 2). In the second step, the thiolate anion of cysteine Cys_{145} S^{-} will then attack the α-keto group of the inhibitor to form a C−S covalent bond and an oxyanion, followed by abstraction of a proton from the nearest base histidine (His_{41}) (Scheme 2). Moreover, as shown in Figure 1, the α-keto group has *Re* and *Si* faces for the nucleophilic reaction. Thus, addition from *Re* and *Si* faces leads to R– and S– stereochemistry adducts. All the adducts, formed by pathways 1–4, caused by the attack from *Si* face and hence have S stereochemistry. Additionally, using SARS-CoV M_{pro}, we also considered the attack of Cys S from *Re* face leading to R-thiohemiketal. However, for the *Re* face reaction, we only examined the reaction by thiolate nucleophile (Cys S^{-}) (Scheme 3). Finally, to find out the stability of R- and S- thiohemiketal and the oxyanion/hydroxyl hole, we will apply modern theoretical tools like NCI-reduced density gradient (NCI-RDG) methods along with Bader's Quantum Theory of Atoms-in-Molecules (QTAIM) and natural bonding orbital (NBO) analysis.

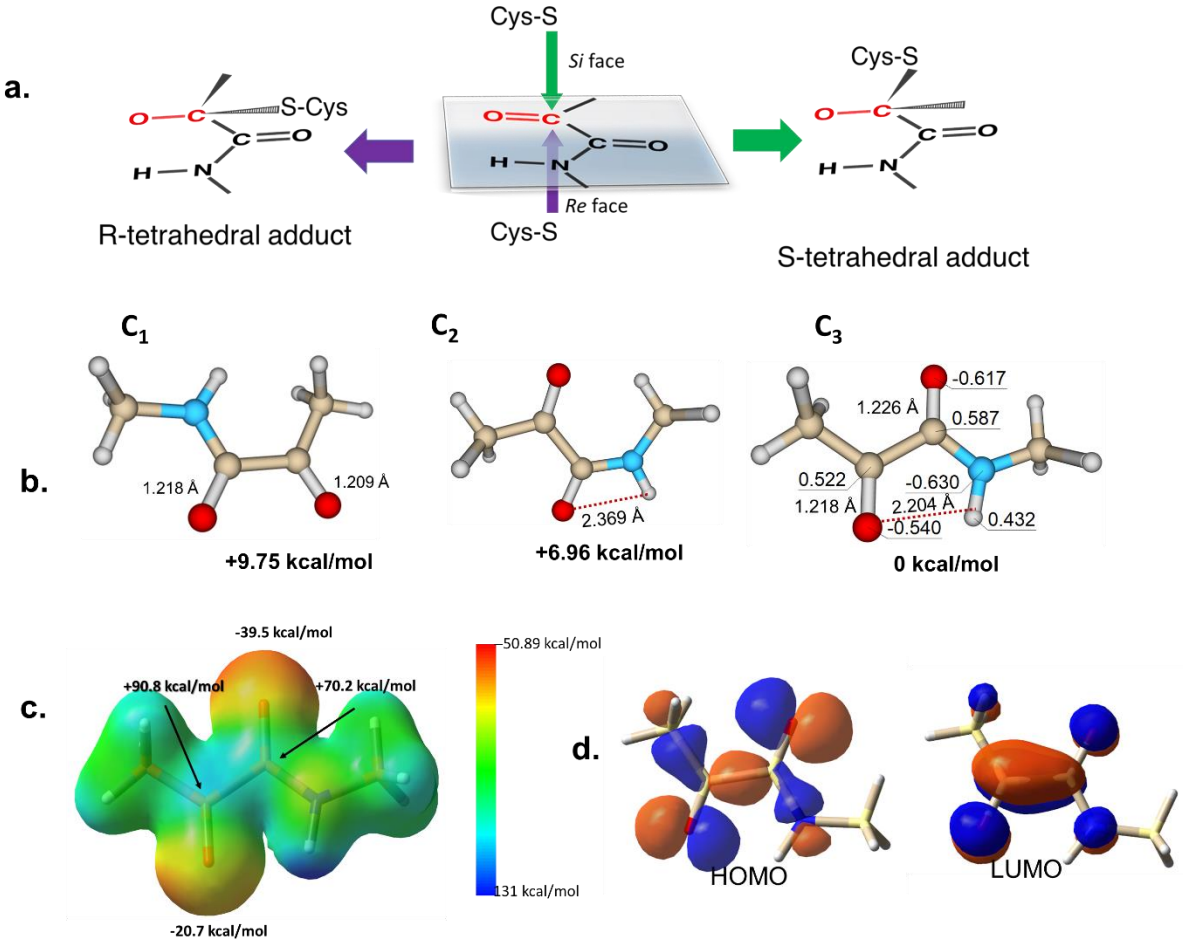

Figure 1. a) Enantioselective reaction between SARS-CoV M_{pro} and α-ketoamide. b) Possible confirmation of α-ketoamide. The labels on conformation C_3 indicates NBO charges in e unit. c) MEP plot of α-ketoamide

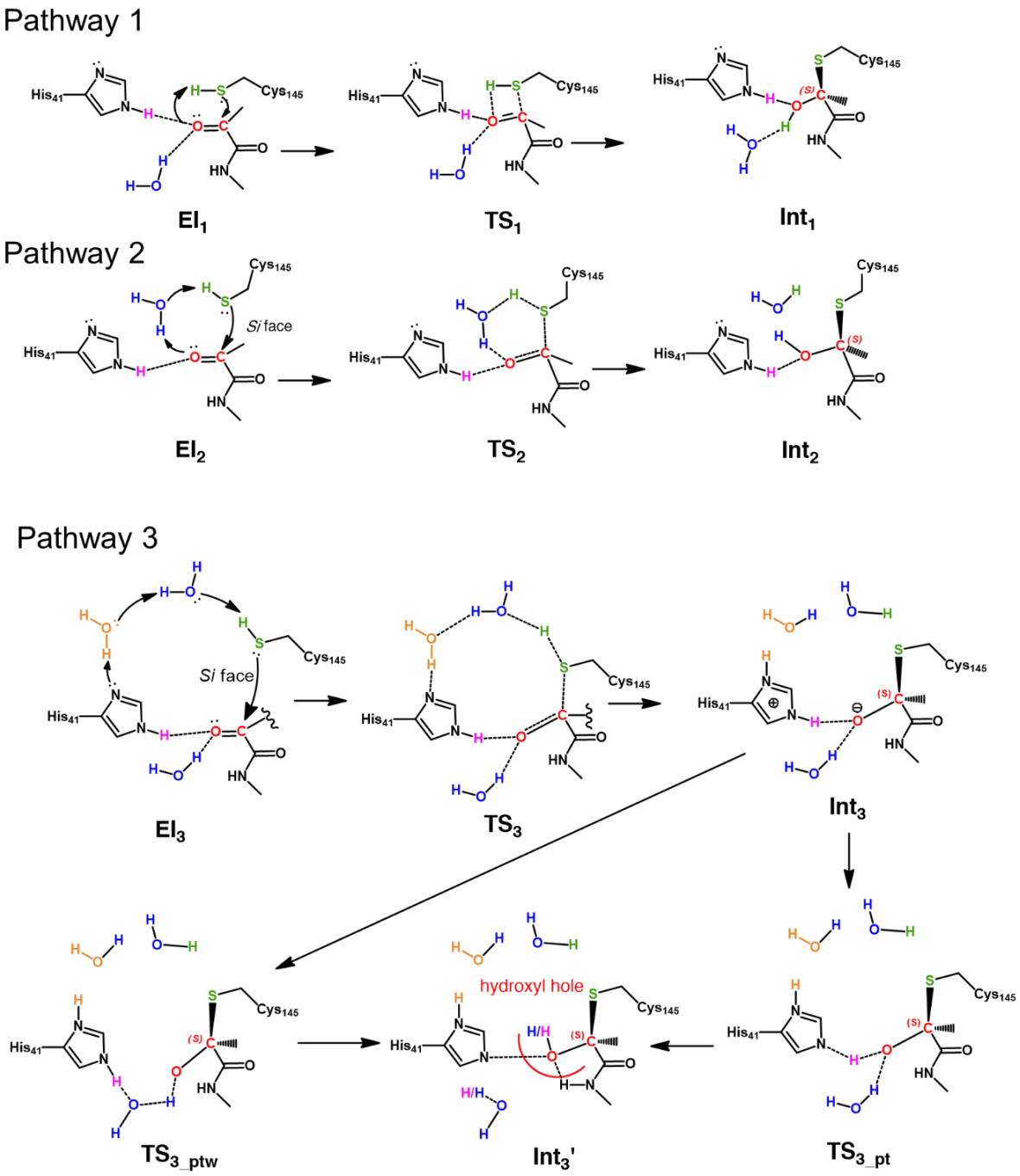

Scheme 1. Proposed concerted reaction mechanism between the active site of SARS-CoV-2 M_{pro} and α-ketoamide inhibitor-warhead from *Si* face based on the present calculations.

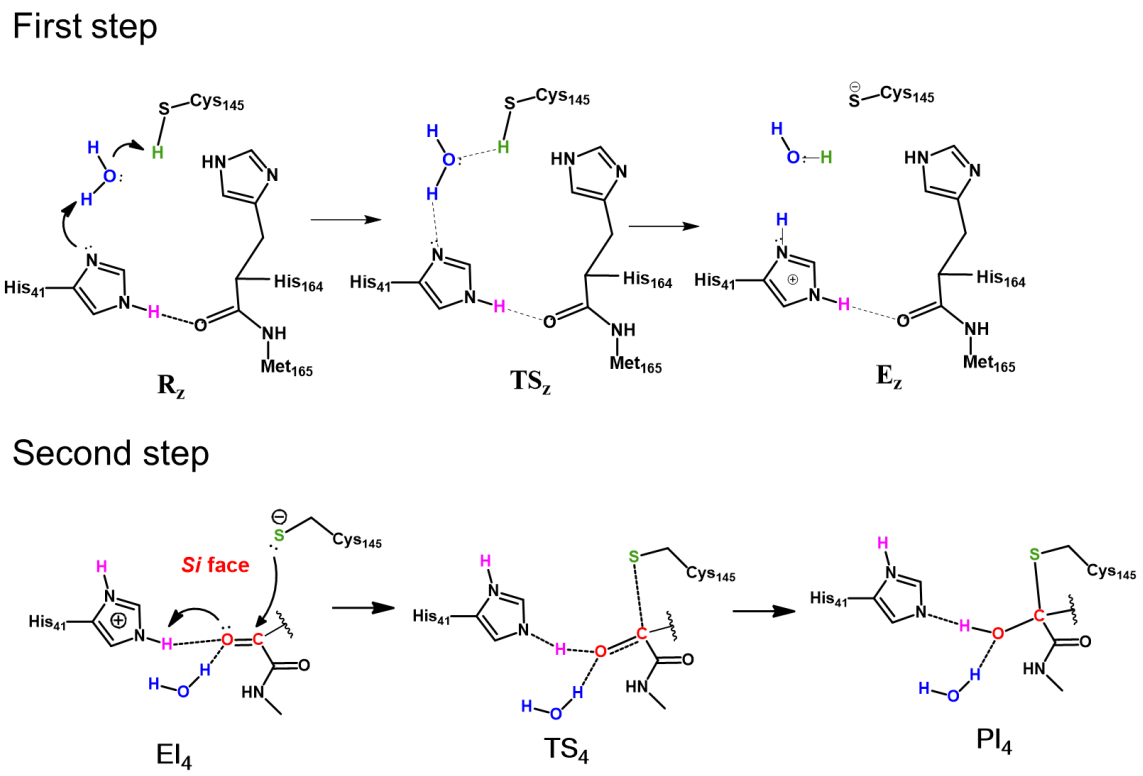

Scheme 2. Proposed two-step reaction mechanism, according to pathway 4, between active site of SARS-CoV-2 M_{pro} with α-ketoamide inhibitor-warhead from *Si* face based on the present calculations.

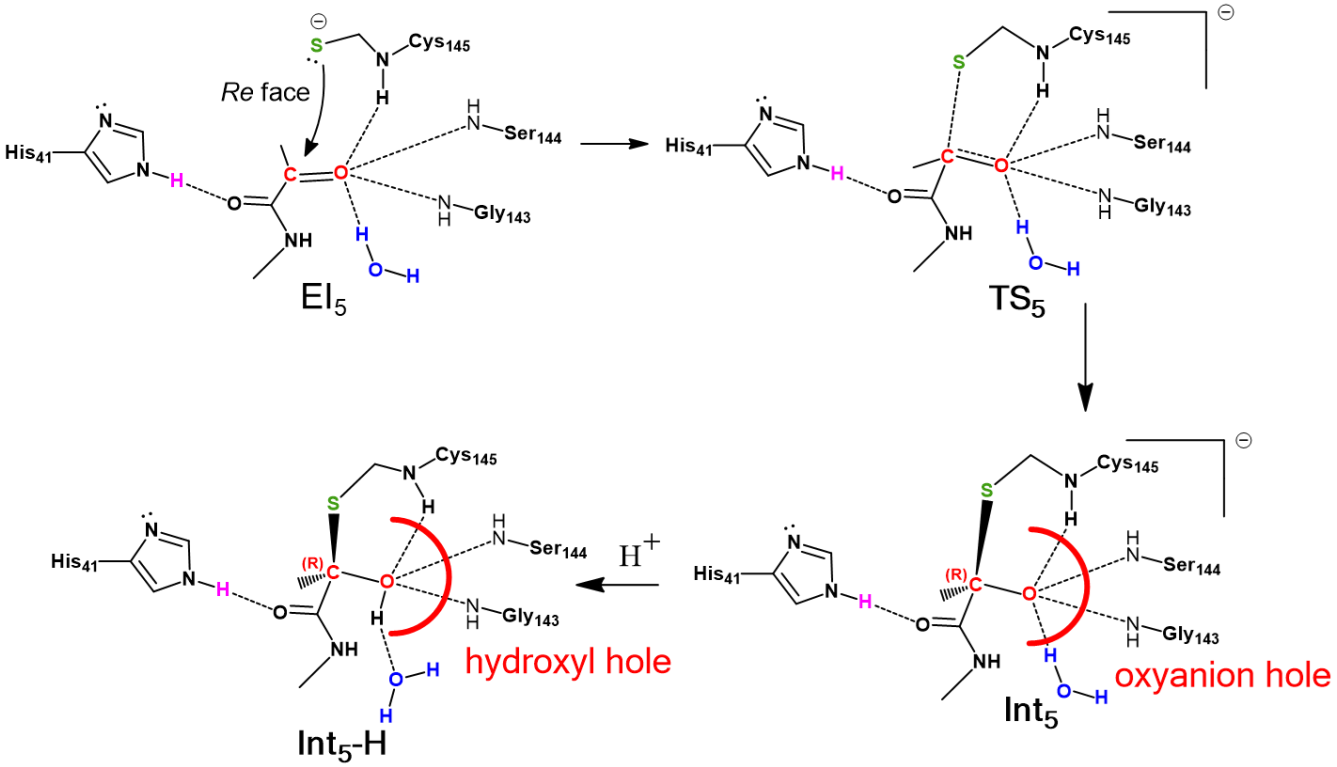

Scheme 3. Proposed two-step reaction mechanism between the active site of SARS-CoV M_{pro} with α-ketoamide inhibitor-warhead from the *Re* face to generate R-thiohemiketal based on the present calculations.

1. METHOD AND COMPUTATIONAL STUDIES

Here, we applied ONIOM-QM/SQM model (QM =quantum mechanical; SQM= semi-empirical QM) treating the protease and inhibitor computationally. In this model, we have considered large number atoms from nearest interacting amino acids as shown in Figure 2. Here, to fulfill the need, we consider only the active species and key hydrogen bonding interactions. We have used hybrid B3LYP[41,42] and Semi-empirical PM6[43] level of theory (ONIOM-B3LYP/6-31G(d):PM6)[44] for optimization. For the more accurate single-point energy calculation, we used dispersion corrected ωB97X-D/6-31G(d,p):PM6 level of theory on the B3LYP/6-31G(d):PM6 optimized geometries. Hydrogens were used as link atoms. We performed all calculations unless indicated otherwise, by using the Gaussian 09 suite of programs.[45] The effect of the low polarity protein environment, on the active-site model, was estimated by performing single-point calculations using the polarizable continuum model (PCM) with UAKS radii[46] method at the same level of theory as the geometry optimizations. The dielectric constant was set to the standard value $\varepsilon = 4$ to represent this environment[47]

The QM/SQM energies were calculated using the following equation as the separate energies of a QM calculation on the QM region (E_{model}, QM) and an SQM calculation on the whole system (E_{real}, SQM) minus an SQM calculation on the QM region (E_{model},MM). The use of such ONIOM model is capable of optimizing and characterizing all critical structures properly along with the energy profile.

The energy is calculated using the following equation:

$$E(ONIOM) = E_{real}(SQM) - E_{model}(SQM) + E_{model}(QM) \quad (1)$$

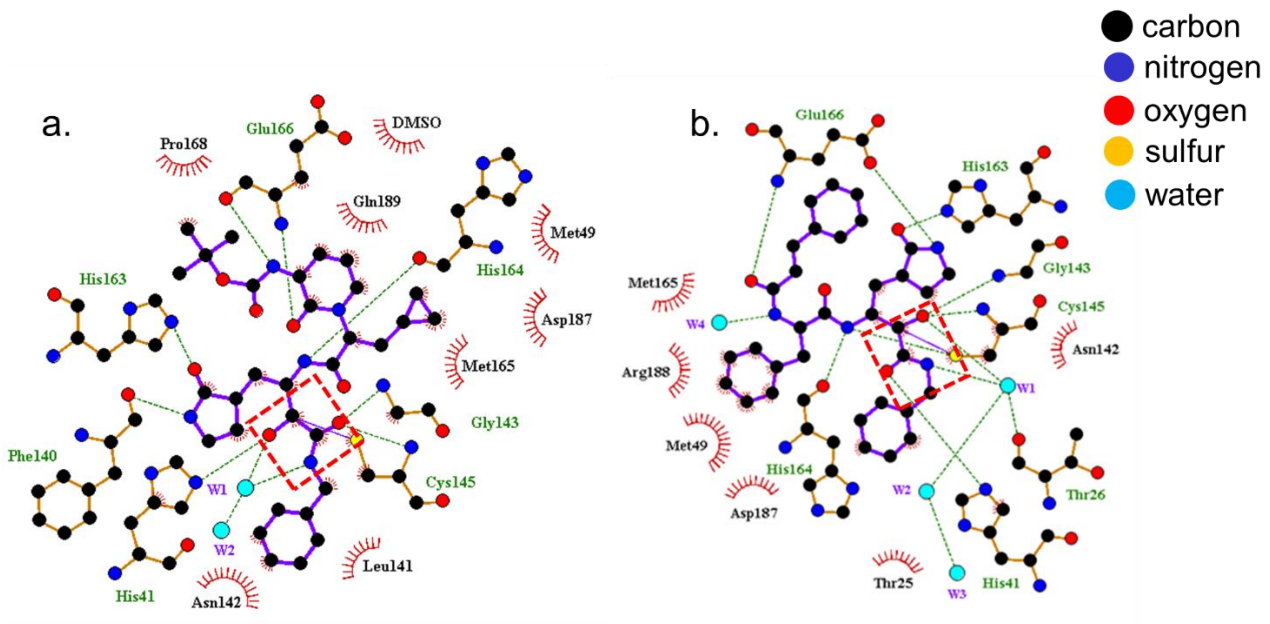

Figure 2. Schematic diagram indicating the atoms of the S- and R-thiohemiketal adducts taken from pdb code a) 6y2f and b) 5n19. Green lines indicate hydrogen bonds. Not all atoms are shown for the sake of clarity. Red rectangles indicate the α-ketoamide inhibitor-warhead of interest in the present paper. The figure is drawn with ligplot.[48]

To explore the activation energy barrier of each step and the energy profile, we optimized all the intermediate and transition state (TS) geometries. We found no imaginary frequencies for the geometries of minima indicating that the obtained stationary points are the lowest-energy points at potential energy surface (PES). On the other hand, only one imaginary frequency at the TS geometry demonstrated that this geometry is a first-order saddle point on the PES. To verify the reliability of the TSs, intrinsic reaction coordinates (IRC) were also computed.

Natural bond orbital (NBO)[49] analysis at B3LYP/6-31G(d) level was carried out to understand the orbital interactions and charge delocalization for the title complexes. In such analysis, NBOs are first defined for each covalent bond, lone pair, and anti-bonding orbital by using the molecular orbitals obtained by quantum-chemical calculations, and the orbital interaction energies are subsequently computed for all possible interactions between electron-donor Lewis-type NBO (i) and acceptor non-

Lewis NBO (j). For each electron-donor NBO (i) and electron-acceptor NBO (j), the stabilization energy E^2_{ij} associated with delocalization i→j is calculated as

$$E^2_{ij} = q_i \frac{F(i,j)^2}{\varepsilon_j - \varepsilon_i} \qquad (2)$$

where q_i is the donor orbital occupancy, ε_i and ε_j are orbital energies, and F(i,j) is the off-diagonal NBO Fock matrix element.

Additionally, we used a powerful tool NCI-RDG method to distinguish and visualize weak interactions: stabilized (hydrogen bonding), destabilized (steric repulsion) and delocalized weak (van der Waals). Specifically, the plot of S and sign(λ2)ρ reveals troughs, which signify the different noncovalent interactions. The troughs corresponding to attractive interactions (such as H-bonds) lie in the region of negative sign(λ2)ρ, whereas repulsive interactions lie in the positive region.

The initial structure of coronavirus protease is extracted from the crystallographic data of the ligand-free enzyme of the SARS-CoV-2 (2019-nCoV) main protease (pdb:6y2e). Furthermore, the initial structure of the enzyme–inhibitor complexes are obtained from the crystallographic data of R– and S–adduct of SARS-CoV and SARS-CoV-2, respectively, main protease and α-ketoamide inhibitor using 6y2f and 5n19 pdb files from the protein data bank.

Now in the simplified model, during optimization, there may be possibilities to collapse the rigid enzyme structure leading to unrealistic structure. To prevent this, we kept some atoms fixed based on the parameters found in the crystal structure. The inclusion of such constrain allows obtaining a more realistic rigid structure. However, such constrain optimization sometimes leads to small frequencies, but here, as the number of frozen atoms is very small, in few structures, we obtained imaginary frequencies, that too below 2 cm^{-1}, and thus neglected.

2. RESULTS AND DISCUSSION

3.1 Structure of the inhibitor-free enzyme and α-ketoamide

As stated above, we started our investigation with the crystal structure of ligand-free M_{pro} (pdb:6y2e). Initially, the protonation and crude optimization were performed using the H++ web server at pH 7.3 to mimic the experimental conditions.[50] Then, we optimized a truncated version of the enzyme by using some active site selected residues including His_{41}, Gly_{143}, Ser_{144}, Cys_{145}, $His_{164,}$ and His_{165}. Our objective is to understand the characteristics and relative strength of hydrogen bonds and other non-covalent interactions occurring in the active part of the enzyme in the absence of the warhead of inhibitor.

Figure S1 (in supporting information) shows that the H-bond network among the residues in the active site creates a pocket large enough to accommodate the α-ketoamide. Also, we detect the other intermolecular interactions as depicted by NCI-RDG isosurface plot (shown in Figure S1b by red arrows) and important bond critical point (bcp) indicating the inter-residual H-bonds, along with a cage critical point (Figure S1c, green sphere).

Additionally, to compare the structure of enzyme-inhibitor complex and inhibitor-free enzyme, we have deleted the inhibitor from the enzyme-inhibitor complex (6y2f) and compare the structure with free enzyme active sites as shown in Figure S2. Aiming to have a complete overview of the α-ketoamide inhibitor, we optimized a simple α-ketoamide N-methyl-2-oxopropanamide. We find that there are three possible isomers of α-ketoamide C_1, C_2, and C_3 (Figure 1b). Obviously, the C_3 isomer is more stable than the other two isomers C_1 and C_2, in this case, by 9.75 kcal/mol computed at b3lyp/6-31G(d) level for the presence of H-bond of 2.20 Å. The natural population analysis (NPA) shows that the natural charge on amidic carbon is +0.58e while that on αC is +0.52e. However, the molecular electrostatic potential (MEP) plot shows that αC is more electrophilic than that of amidic carbon. The results show that HOMO-LUMO energy gap of this molecule is 4.86 eV and the isosurface plot of HOMO and LUMO are depicted in Figure 1d. Interestingly, the LUMO of S-In contains the π* orbital for accepting nucleophile, while in R-In, the π* orbital is located on LUMO+1 (See Figure S3).

3.2 Reaction Mechanism of α-ketoamide with M_{pro} from *Si* face to form S-thiohemiketal

***Pathway 1*: Concerted self-catalyzed reaction without water and histidine as a function of the shuttle.** In this mechanism, first, a non-covalent enzyme-inhibitor complex **EI$_1$** is formed. Then, this complex proceeds to form a tetrahedral complex (**Int$_1$**) *via* a transition state (**TS$_1$**), by nucleophilic attack of Cys_{145} S onto αC atom, with a simultaneous transfer of a proton from SH to O. We optimized all these geometries (Figure 3) and for only **TS$_1$**, we found one imaginary frequency of −1332 cm^{-1} indicating a sharp TS, while no imaginary frequencies are observed for **EI$_1$** and **Int$_1$**. In **EI$_1$**, the S−H and C=O bonds are oriented in parallel, with Cys_{145} S atom pointing at αC and thiol H atom pointing at O(αC) atom. The S−αC and H−O(αC) bond distances are 2.23 and 2.55 Å, respectively. We identified a bond critical point bcp between incoming S and electrophilic αC by applying QTAIM analysis. The electron density (ρ), Laplacian of electron density ($\nabla^2\rho$), and energy density (H(r)) are 0.0479, 0.2949, and −0.0068 a.u. The positive sign of $\nabla^2\rho$ and negative sign of H(r) supports a non-covalent nature of the S−αC interaction. We find a donor-acceptor NBO pair $n_S \rightarrow \pi^*_{C=O}$ with delocalization energy of E^2 = 50.4 kcal/mol. NBO charge analysis also shows that the natural charge on sulfur increases from 0.213e in **EI1** to 0.254e in **TS1**, and subsequently, on the O(αC), the negative charge increases from −0.332e (in **EI1**) to −0.357e in **TS1** indicating a charge transfer from Cys_{145} moiety to the α-ketoamide. In **TS$_1$**, these bond distances are reduced to 1.92 and 1.43 Å, respectively. At **TS1**, two important NBO pairs are detected (Table S1 and Figure 4): the first one is $n_{O(\alpha C)} \rightarrow \sigma^*_{S-H}$ which indicates the S-H bond cleavage O-H bond formation, and the second one $n_{O(\alpha C)} \rightarrow \sigma^*_{N\delta-H}$ supports that His_{41}, by forming H-bonds with O(αC), helps to make the αC more electrophilic and thus more susceptible to the nucleophilic attack (Figure 3). The geometry at αC changes from planar to tetrahedral as the reaction proceeds from **EI$_1$** to **TS$_1$** to **Int$_1$**. In **Int$_1$**, the values of ρ, $\nabla^2\rho$, and H(r) at the bcp on S−αC bond are 0.1631, −0.2526 , and −0.1336. The negative sign of $\nabla^2\rho$ and H(r) indicates the covalent nature of C−S bond. The energy barrier (E_{act}) for this mechanism is 21.0 kcal/mol computed at ωB97X-D/6-31G(d,p)//B3LYP/6-31G(d):PM6 and the reaction are

exoergic, $\Delta_rE \approx 25.1$ kcal/mol. However, in the protein environment at $\varepsilon = 4$, the energy these values are lowered, for example, E_{act} and Δ_rE are *ca.* 19.1 and −13.1 kcal/mol, respectively (Figure 5 and Table 1).

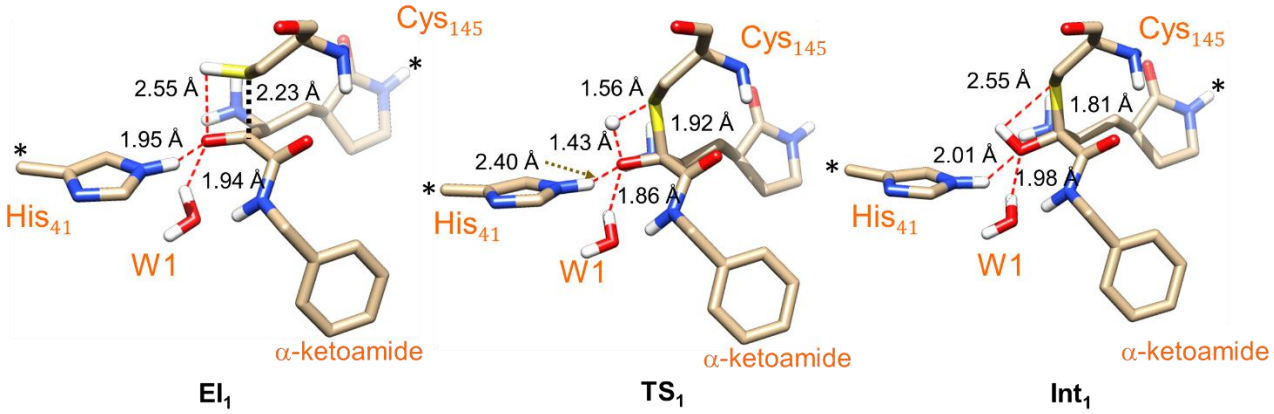

Figure 3. Optimized geometries of the intermediates and transition state of the concerted self-catalyzed reaction (as in Pathway 1) between M_{pro} and α-ketoamide of the inhibitor from *Re* face. Atoms marked with asterisks are fixed during geometry optimization. For the sake of clarity, only polar hydrogen atoms are shown.

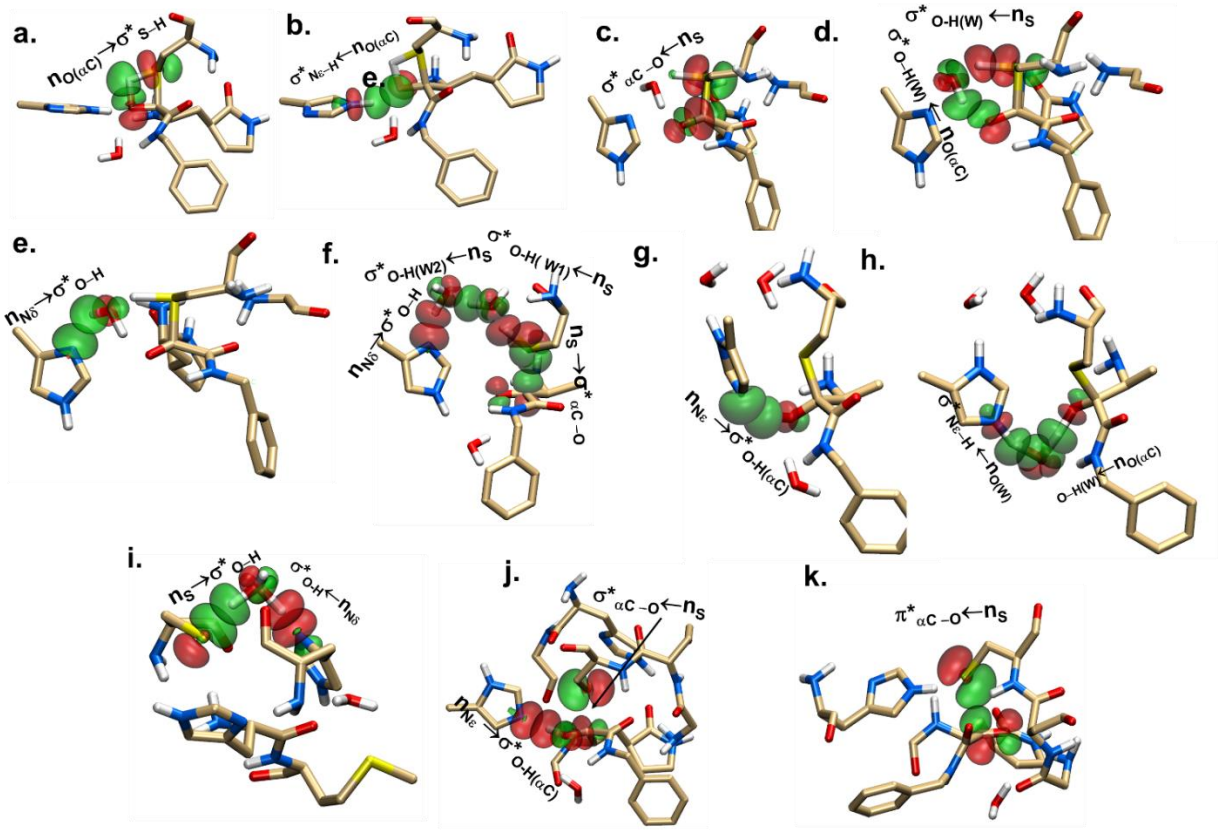

Figure 4. The donor–acceptor NBOs of transition states involved in the proposed mechanism according to different pathways: i) **TS_1** : a and b, ii) **TS_2**: c, d, and e, iii) **TS_3**: f, iv) **TS_{3_pt}**: g, v) **TS_{3_ptw}**: h, vi) **TS_z**: i; vii) **TS_4**: j, viii) vii) **TS_5**: k.

Table 1. Activation parameres and the reaction energies (kcal/mol) of investigated paths explored in the present study in the gas phase and PCM media at $\varepsilon = 4$[a]

	gas phase			$\varepsilon = 4$		
	$\Delta E_{act(forward)}$	$\Delta E_{act(reverse)}$	$\Delta_r E$	$\Delta E_{act(forward)}$	$\Delta E_{act(reverse)}$	$\Delta_r E$
TS_1	21.0	46.1	–25.1	19.1	32.4	–13.3
TS_2	2.0	29.7	–27.7	1.8	6.0	–4.2
TS_3	4.9	13.4	–8.5	-1.0	2.8	–3.8
TS_{3_pt}[b]	2.4 (10.9)	12.3	–1.4	14.2 (18.0)	20.4	1.4
TS_{3_ptw}[b]	2.5 (11.0)	12.4	–1.4	2.9(6.7)	5.3	1.4
TS_z	12.1	13.2	–1.1	2.5	15.6	–13.1
TS_4	1.0	20.2	–19.2	1.0	10.9	–9.9
TS_5	4.8	6.0	–1.2	6.8	31.6	–24.8

[a]All $\Delta E_{act(forward)}$ and $\Delta_r E$ values are relative to their corresponding enzyme-inhibitor non-covalent complexes, for example, for TS_1, the results are relative to EI_1. The $\Delta E_{act(reverse)}$ values are relative to their corresponding enzyme-inhibitor covalent complexes, for example, for TS_1, $\Delta E_{act(reverse)}$ value is calculated relative to Int_1. [b]data within the bracket are relative to Int_3.

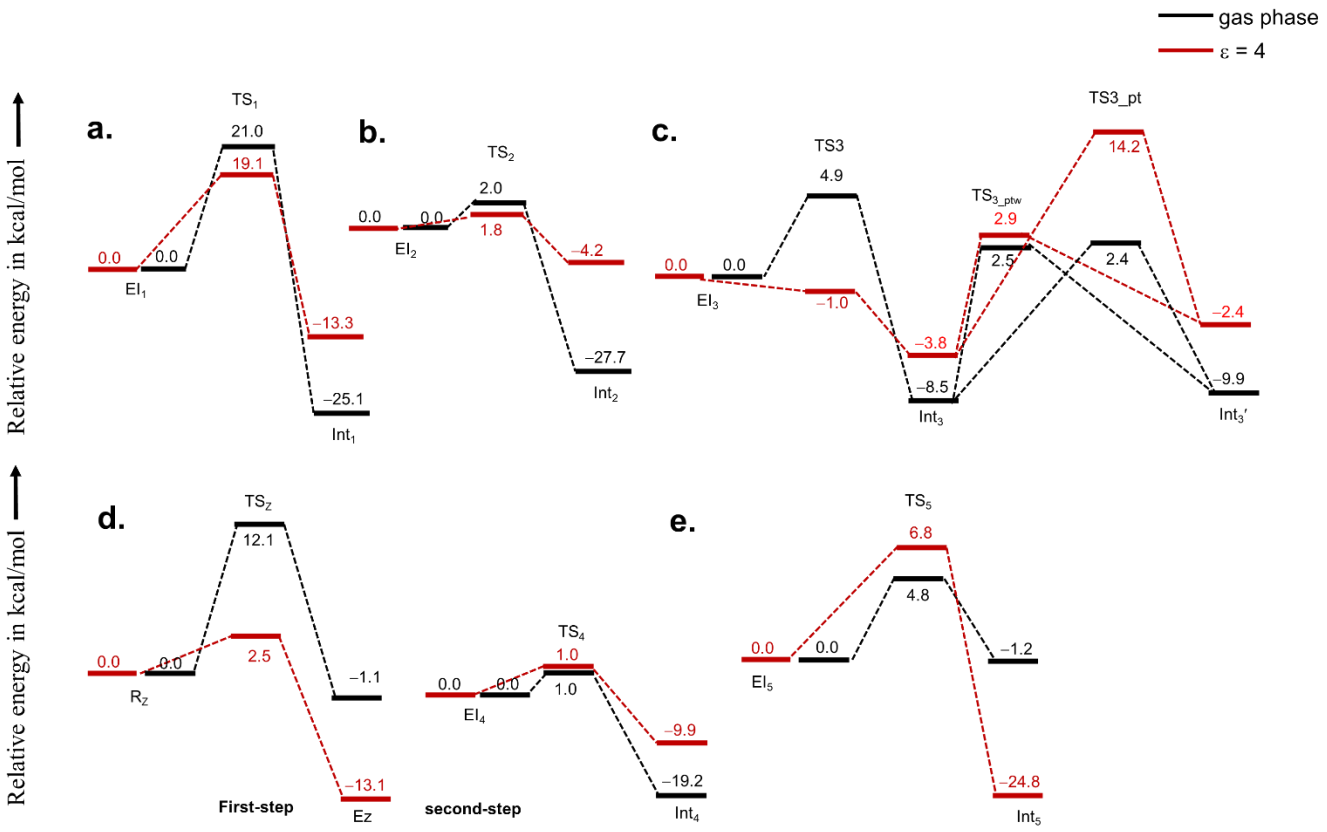

Figure 5. Calculated energy profiles of all the pathways for R– and S–thiohemiketal according to a) pathway 1, b) pathway 2, c) pathway 3, d) pathway 4, and e) reaction from *Re* face according to scheme 3.

***Pathway 2*: Concerted water-assisted reaction without histidine as a function of a shuttle**

To model this approach, we propose that the reaction started from the initial inhibitor-enzyme complex **EI$_2$**, which is formed by the interaction active site amino acids and inhibitor. Herein, a water molecule serves as a shuttle to transfer proton of Cys$_{145}$ SH to α-keto oxygen. As the reaction proceeds, **EI$_2$** transforms to tetrahedral-intermediate **Int$_2$** *via* the 6-membered transition state **TS$_2$**. The **TS$_2$** is characterized by an imaginary frequency of –567 cm^{-1}, and the imaginary mode clearly identified that the TS corresponds to the synchronous process of proton transfer and nucleophilic attack. Importantly, here, His$_{145}$ functions as an H-bond donor and not as a proton shuttler. The optimized geometries along with important geometrical parameters of **EI$_2$**, **TS$_2$**, and **Int$_2$** are shown in Figure 6. In **EI$_2$**, the critical S-αC distance is 2.07 Å and becomes shorter to reach 1.96 Å at **TS$_2$** and 1.88 Å in **Int$_2$**. In **EI$_2$**, we find a bcp

between S and αC with ρ and $\nabla^2\rho$ values of 0.0923 and 0.4328 a.u. The non-negative value of $\nabla^2\rho$ supports the non-covalent interaction of S and αC. On the other hand, in **Int$_2$**, the negative values of $\nabla^2\rho$ and H(r) are indications of the covalent nature of C–S bond. In **TS$_2$**, the water molecule is assisting the proton-transfer by bridging between O(αC) and Cys$_{145}$ S, with two H-bonds of 1.64 and 1.50 Å, respectively.

The NBO analysis shows that, in **EI$_2$**, the main donor–acceptor NBOs $n_S \rightarrow \pi^*_{\alpha C=O}$ (E^2 = 101.4 kcal/mol) clearly indicates the attack of Cys$_{145}$ S to αC of ketoamide (Figure 4). Also, in **TS$_2$**, we properly identified three main donors –acceptor NBO pairs $n_S \rightarrow \sigma^*_{\alpha C=O}$, $n_S \rightarrow \sigma^*_{O-H(W)}$, and $n_{O(\alpha C)} \rightarrow \sigma^*_{O-H(W)}$ indicating the participation of water in the transition states (See Figure 4 and Table S1). Furthermore, the NBO charge analysis shows that, in the conversion of **EI$_2$** to **TS$_2$**, the charge transfer on S is not significant, whereas, the negative charge on O(αC) changes from –0.339e to –0.440e indicates that the protonation of O(αC) initiates the nucleophilic attack. However, we note that, in this pathway, the overall resemblance between **Int$_2$** and crystallographic structure (See Figure 6 and 10, later) is not good. For example, S–C distance in **Int$_2$** is 1.88 but the crystallographic distance is 1.81 Å. Similarly, there a moderate disagreement in the H-bond network between the His$_{41}$ and tetrahedral-intermediate. The calculated energy of **TS$_2$** is 2.0 kcal/mol in the gas phase and 1.8 kcal/mol at ε = 4 relative to **EI$_2$** (Figure 5 and Table 1). This step is also highly exoergic of –27.5 and –4.2 kcal/mol in the gas phase and 4, respectively.

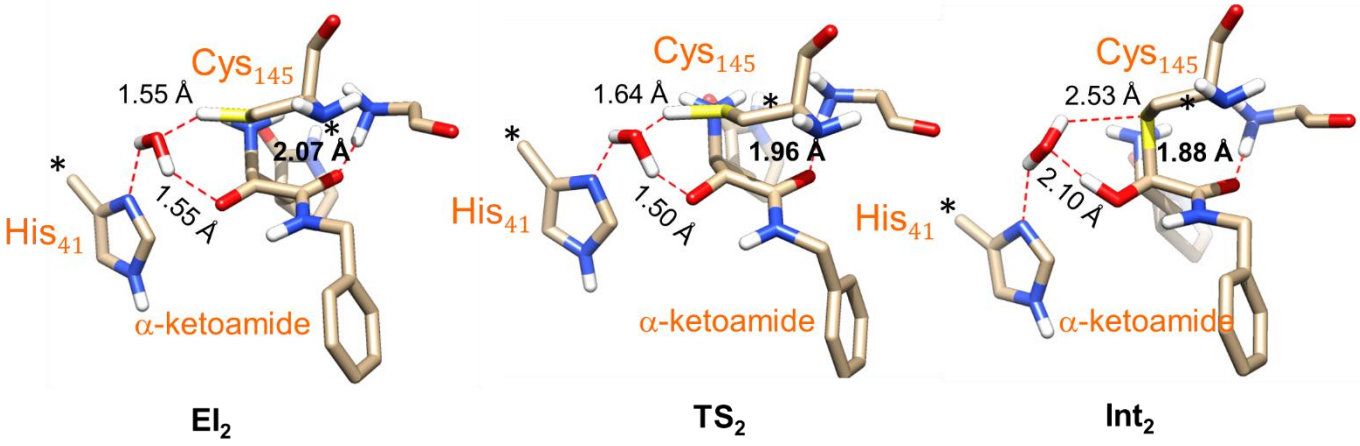

Figure 6. Optimized geometries of the intermediates and transition state of the concerted water-assisted reaction (as in Pathway 2) between M_{pro} and α-ketoamide of the inhibitor from Re face. Atoms marked with asterisks are fixed during geometry optimization. For the sake of clarity, only polar hydrogen atoms are shown.

***Pathway 3*: Concerted reaction with two water and histidine as a function of shuttle**

In this approach, we assumed that the concerted proton transfer and nucleophilic attack is assisted by two water molecules and the nearby neutral Nε protonated His_{41} residue (see Scheme 1). The optimized structure of the enzyme–inhibitor complex **EI₃** is shown in Figure 7. In **EI₃**, two water molecules bridges between Cys_{145} SH and His_{41} δNH with three H-bonds of 1.75, 1.31, and 1.47 Å. The reactant proceeds from **EI₃** to **Int₃** *via* **TS₃**. We detect a bcp at **EI₃**, between S and α C with ρ, $\nabla^2\rho$, and H(r) values of 0.0540, 0.3303, and –0.0121 a.u., indicating non-covalent nature of the bond. To support from NBO study, we find a donor–acceptor NBO pair $n_S \rightarrow \sigma^*_{\alpha C=O}$ of E^2 = 57.1 kcal/mol. The optimized **TS₃** is characterized by an imaginary frequency of 208*i* cm^{-1}. The vibrational movement at imaginary mode indicates the simultaneous transfer of a proton from Cys_{145} SH to His_{41} δN *via* two bridging water molecules W_1 and W_2 together with the nucleophilic attack by the Cys_{145} SH onto the αC of the inhibitor. Additionally, the donor–acceptor properties, involved in **TS₃**, are well supported by the NBO analysis (Figure 4). We find that, in **TS₃**, four important NBO pairs, namely, $n_S \rightarrow \sigma^*_{O-H(W1),}$ $n_{O(W1)} \rightarrow \sigma^*_{O-H(W2),}$ $n_{N\delta} \rightarrow \sigma^*_{O-H(W2),}$ and $n_S \rightarrow \sigma^*_{\alpha C-O}$ well supports the donor and acceptor atoms. The optimized geometries show that the main distance S–αC in reduces from 2.23 Å at **EI₃** to 2.18 Å in **TS₃**, 1.97 Å in

Int$_3$, and 1.83 Å in **Int$_3$′**, and consequently, the αC–O$^-$ increases from 2.22 to 2.24 to 2.28 to 2.41 Å. Furthermore, **Int$_3$** is a tetrahedral oxyanion-intermediate stabilized by three H-bonds: His$_{41}$ εH···O$^-$, W$_3$ H···O$^-$, and intramolecular α-amidic H···O$^-$ with 2.16, 1.76 and 2.31 Å, respectively. Similar to the previous pathways, here also, the non-covalent S–C bond becomes covalent in **Int$_3$** ($\nabla^2\rho \approx -0.2321$, H(r) ≈ –0.1240 a.u.). The energy barrier for this step shows 4.9 kcal/mol relative to **EI$_3$** in the gas phase. While the reaction is barrierless (E_{act} = –1 kcal/mol) at the protein environment ε = 4 (Table 1). Finally, the intermediate **Int$_3$** converts to **Int$_3$′** by transferring a proton from His$_{41}$ δN to oxyanion formed by αC. We consider two paths for such proton transfer: direct and water-mediated, and consequently, we obtained two corresponding transition states **TS$_{3_pt}$** and **TS$_{3_ptw}$** as shown in Figure 7. **TS$_{3_pt}$** and **TS$_{3_ptw}$** are characterized by the imaginary frequencies of 416*i* and 313*i* cm^{-1}, respectively. The transition state **TS$_{3_pt}$** shows that the transferring proton is exactly shared by the imidazole Nδ of His$_{41}$ and the oxyanion. In **TS$_{3_pt}$**, we detect an NBO pair $n_{N\delta} \rightarrow \sigma^*_{O-H}$ of E^2 = 230.1 kcal/mol to support the donor–acceptor properties. In **TS$_{3_ptw}$**, the two important NBO pairs are $n_{O(W3)} \rightarrow \sigma^*_{N\varepsilon-H}$ and $n_{O(\alpha C)} \rightarrow \sigma^*_{O-H(W3)}$ with delocalization enrgy of 149.6 and 263.1 kcal/mol. Energy profile diagram shows that proton transfer for *via* **TS$_{3_ptw}$** is more preferable (E_{act} ≈ 2.9 kcal/mol) than *via* **TS$_{3_pt}$** (E_{act} ≈ 14.2 kcal/mol) in protein environment at ε = 4. Furthermore, the results indicate that, in the gas phase, the ion pair **Int$_3$** is less stable, by *ca.* 1.4 kcal/mol, than its neutral counterpart **Int$_3$′** while the reverse is true in continuum solvent model, that is, at ε = 4, **Int$_3$** is more stable than **Int$_3$′** by *ca.* 1.4 kcal/mol. In **Int$_3$′**, the S–αC distance is 1.83 Å. The computed structure of **Int$_3$′** almost resembles the crystallographic structure within the full enzyme environment.

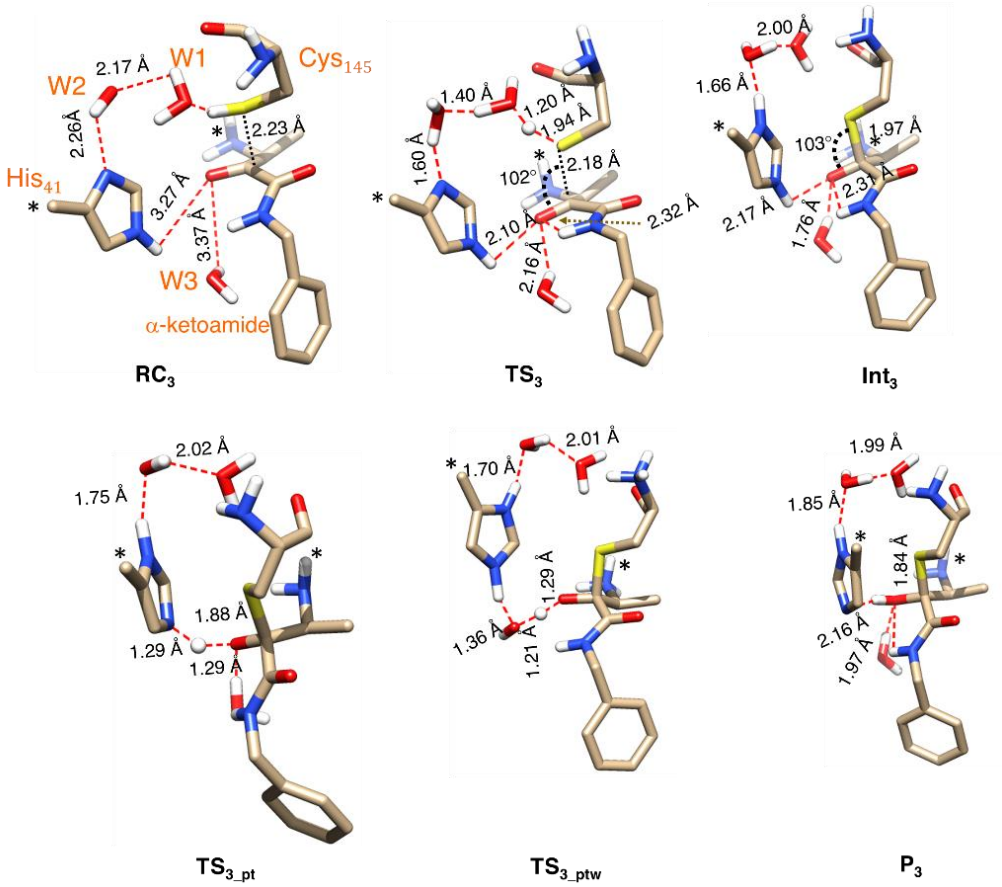

Figure 7. Optimized geometries of the intermediates and transition state of the concerted reaction according to Pathway 3 between M_{pro} and α-ketoamide of the inhibitor from *Re* face. Atoms marked with asterisks are fixed during geometry optimization. For the sake of clarity, only polar hydrogen atoms are shown.

***Pathway 4*: Stepwise process using histidine as proton donor-acceptor**

First-step: As stated in the introduction, the first step is the proton transfer from Cys_{145} SH to Nε protonated His_{41} Nδ. Before starting the calculation, for correct protonation site and fixing any missing atoms at experimental pH 7.3, we run the crystallographic molecule in H++ server. The results show that, in the crystal, the distance between Cys_{145} sulfur and His_{41} Nδ (S ⋯ Nδ) is 4.94 Å, and this is too large to transfer. The results of H++ server also show that the S–H bond is oriented in such a direction from where the proton transfer is not possible. Besides, as the nearest water molecule, H_2O_{637} (in pdb:6y2e), is 3.49 Å away from the Nε atom of His_{41}, to overcome the problem, we include an explicit water molecule in the proton transfer. Therefore, herein, a water-mediated proton transfer is assumed to occur. Figure S2

shows that there is a rotation of the imidazole ring to accept the inhibitor. Thus, it can be hypothesized that, in the presence of inhibitor, because of the rotamer of either the imidazole ring of His_{41} or C–S of Cys_{145} (as shown in Figure S4) or by both, the distance between the donor atoms Cys S and His Nδ becomes 3.54 Å. This distance favors the proton transfer to form $CysS^{-}/HisH^{+}$ ion pair. To optimize and characterize all critical structures properly along with the energy profile and to find the transition state as a first-order saddle point, we used the minimum number of proteins as in the catalytic triad (His_{41}, $Cys_{145,}$ and His_{164}) along with Met_{165} and two water molecules (W_1 and W_2). We define the reaction proceeds from the reactant complex (**R**$_z$) to the ion-pair product complex **E**$_z$ *via* the transition state (**TS**$_z$). As shown in Figure 8, in optimized **R**$_z$, the water molecule W_1 connects the donor atoms Cys_{145} S and His Nδ with two H-bonds of 1.69 and 2.04 Å, respectively, by forming a bridge. The transition state **TS**$_z$ is characterized by an imaginary frequency of –117 cm^{-1}. In **TS**$_z$, the bridging W_1 has two O–H distances of 1.26 and 1.17 Å. The S–H distance is increased from 1.40 Å in **R**$_z$ to 1.68 Å in **TS**$_z$ to 3.09 Å in **E**$_z$. The animation of imaginary mode surely indicates the transfer of the proton from donor to acceptor. Also, in the TS, the NBO pairs $n_S \rightarrow \sigma^*_{O-H}$ and $n_{N\delta} \rightarrow \sigma^*_{O-H}$ clearly shows that proton transfer from Cys_{145} SH to His_{41} δN (Figure 4 and Table S1)

The activation barrier of the proton transfer is about 2.5 kcal/mol at ε = 4, while this value is high (12.1 kcal/mol) in the gas phase (Table 1 and Figure 5). The process is an exoergic process of about –13.1 kcal/mol at ε = 4. These results are in agreement with the previously reported data for another similar inhibitor.[28]

Second-step: In this step, the Cys_{145} thiolate ion, formed in by the previous step, attacks the α-keto of the inhibitor to form a C–S covalent bond. In this model, to find the reaction profile, we increase S–C distance gradually, as the reaction coordinate, from 1.73 Å to 3.30 Å with an increment of 0.1 Å at each step (Figure S5). The result shows that the guess transition structure is at about 2.22–2.23 Å and accordingly, we found the correct transition state **TS**$_4$, which is characterized by an imaginary frequency of 109*i* cm^{-1}.

Unfortunately, from the IRC calculation, we could not obtain the initial enzyme–inhibitor complex **EI$_4$**. From the S–C surface scan, we assumed **EI$_4$** that resides very close to **TS$_4$** in the PES, and thus, we optimized **EI$_4$** with a constant distance of 2.33 Å. The optimized structures of the stationary points are shown in Figure 8. In **EI$_4$**, the α-keto oxygen is stabilized by a strong hydrogen bond of 1.69 Å from His$_{41}$ Nε. Also, one crystalline water molecule stabilizes the amidic oxygen to make the αC more electrophilic. Notably, the animation of imaginary mode shows that, at the TS, the attacking of Cys$_{145}$ and transfer of a proton from His$_{41}$ Nε to α-keto oxygen occurs synchronously. Additionally, we find two main NBO pairs $n_S \rightarrow \sigma^*_{\alpha C-O}$ and $n_{N\varepsilon} \rightarrow \sigma^*_{O-H}$ to support the donor–acceptor properties (Figure 4 and Table S1). Finally, **TS$_4$** converts to tetrahedral thiohemiketal **Int$_4$**, where the S–αC bond distance becomes 1.83 Å from 2.22 Å in **TS$_4$**. Consequently the αC–O increases from 1.24 to 1.33 to 1.39 Å as the reaction proceeds from **EI$_4$** → **TS$_4$**→ **Int$_4$**. Here also, the covalent nature of **Int$_4$** is confirmed from their $\nabla^2\rho$, and H(r) values, –0.1663 and –0.0922 a.u. The results show that all the structural parameters of **Int$_4$** resemble well the crystallographic data (Figures 8 and 10). The energy barrier of the step is low *ca.* 1 kcal/mol both at ε = 1 and 4. The conversion **EI$_4$** → **Int$_4$** is exothergic of –9.9 and –19.2 kcal/mol in the gas phase and ε= 4, respectively.

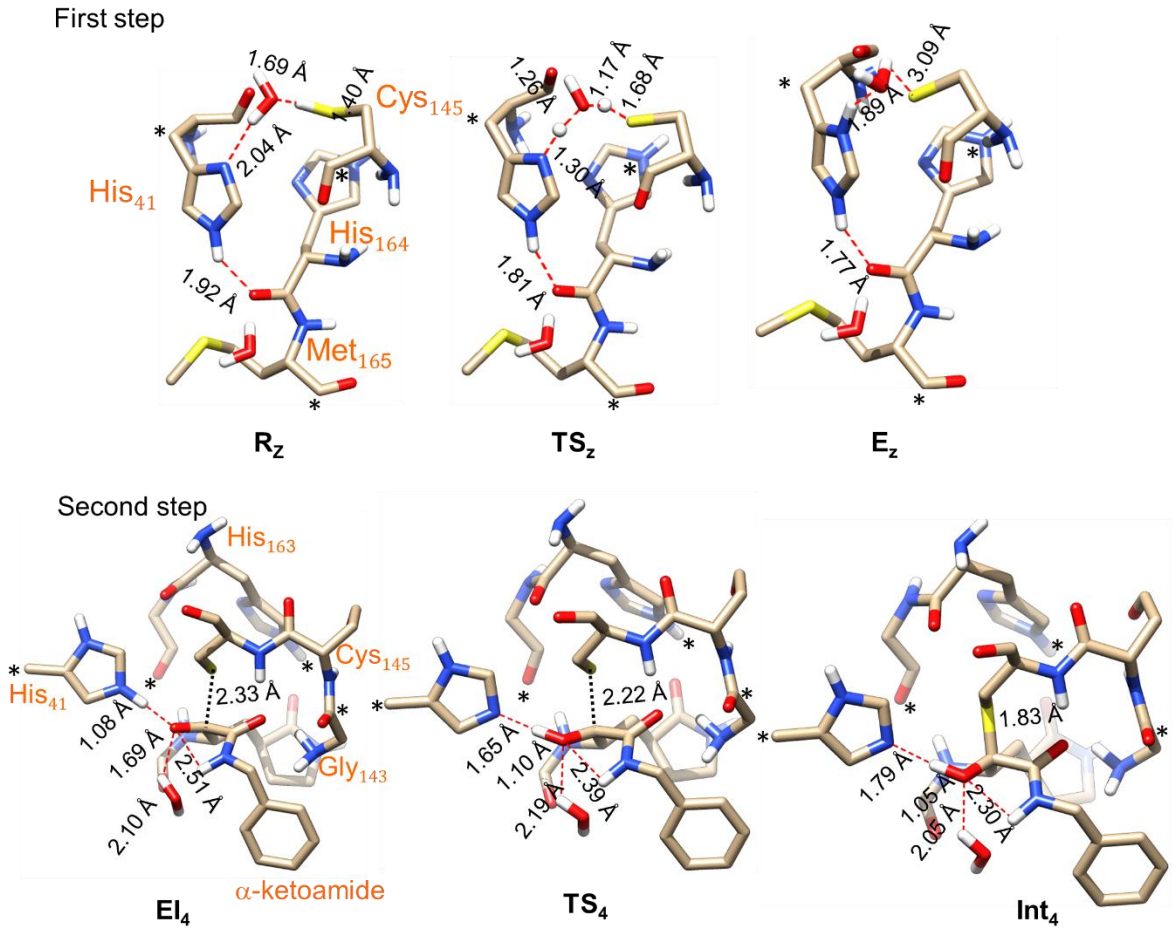

Figure 8. Optimized geometries of the intermediates and transition state of the two-step concerted reaction according to Pathway 4 between M_{pro} and α-ketoamide of the inhibitor from *Si* face. Atoms marked with asterisks are fixed during geometry optimization. For the sake of clarity, only polar hydrogen atoms are shown.

3.3 Reaction Mechanism of α-ketoamide with M_{pro} from *Re* face to form R-thiohemiketal

To model this reaction mechanism, we used the crystal structure of SARS coronavirus main protease in complex with the alpha-ketoamide of R-thiohemiketal (pdb:5n19). We assume that the reaction started from the initial enzyme–inhibitor complex **EI5** (Figure 9). Compare to the Si face reaction with CoV-2 M_{pro}, here, S…C distance is significantly longer, *ca.* 3.09 Å. To verify whether S and αC are in fact interacting or not, we detect a bcp between them with ρ, $\nabla^2\rho$, and H(r) values are 0.0048, 0.0381, and 0.0024 a.u. Besides, we detect a donor–acceptor NBO pair $n_S \rightarrow \pi^*_{\alpha C-O}$ with low delocalization energy of 8.3 kcal/mol. Both the QTAIM and NBO analysis indicates that the interaction between Cys S and αC is very weak and non-covalent in nature. Interestingly, as the Cys_{145} thiolate approaches the α-keto of the

inhibitor from *Re* face, both the attacking nucleophile and the electrophilic-warhead, experience completely different interacting sites from the *Si* face reaction. For example, in **EI$_5$**, amide oxygen is stabilized by His$_{41}$ Nε with a H-bond of 2.36 Å. Similarly, the oxygen of α-keto group is stabilized by the H-bonds from the donor atom of Cys$_{145}$, Gly$_{143}$, and one water (W$_1$) with bond distances of 2.90, 2.23, and 2.38 Å, respectively. The reaction proceeds from **EI$_5$** to transition state **TS$_5$** to tetrahedral intermediate **Int$_5$**. The transition state is characterized by one imaginary frequency of 81*i* cm^{-1} and the animation of the imaginary mode correctly corresponds to the nucleophilic attack of S$^-$ on αC. We find an NBO pair $n_S \rightarrow \pi^*_{\alpha C-O}$ to support the direction of electron migration at TS (Figure 4 and Table S1). With the progress of the reaction, the main distance S–αC decreases from 3.09 Å in **EI$_5$** to attain 2.59 Å in **TS$_5$**, and 1.89 Å in **Int$_5$**, and thereby, the change of hybridization at αC is from sp^2 to sp^3 to form an oxyanion hole (which we will discuss later in detail). Consequently, the αC–O$^-$ increases from 2.21 (in **EI$_5$**) to 2.22 (in **TS$_5$**) to 2.30 Å (in **Int$_5$**), however, this is not shown in Figure 9 for clarity. The optimized structure of **Int$_5$** shows that the oxyanion is stabilized by strong H-bonds from Cys$_{145}$, Gly$_{143}$, and W$_1$ of 1.66, 2.07, and 1.71 Å, respectively. Notably, as stated above, **Int$_5$** has R-stereochemistry. At Int$_5$, the values of $\nabla^2\rho$, and H(r) of bcp are negative which again supports the covalent nature of S–C bond. To verify the validity of the computed results, we protonated and optimized the oxyanion of **Int$_5$** (named as **Int$_5$-H)**, and compared it with the crystallographic result. The computed results resemble closely that of the experimental data. For example, the main covalent bond distance S–αC is 1.82 in **Int$_5$-H** is good agreement with the experimental data 1.80 Å.[1] Also, all the H-bonds are in close agreement with the crystallographic data as shown in Figure 9 and 10. The energy barrier this reaction is 4.6 kcal/mol in gas phase and 6.8 at ε = 4 (Figure 5 and Table 1). Like the reaction from *Si* face, here also, the reaction is exoergic of 24.8 kcal/mol in enzyme environment. However, in the gas phase, exoergicity is lowered.

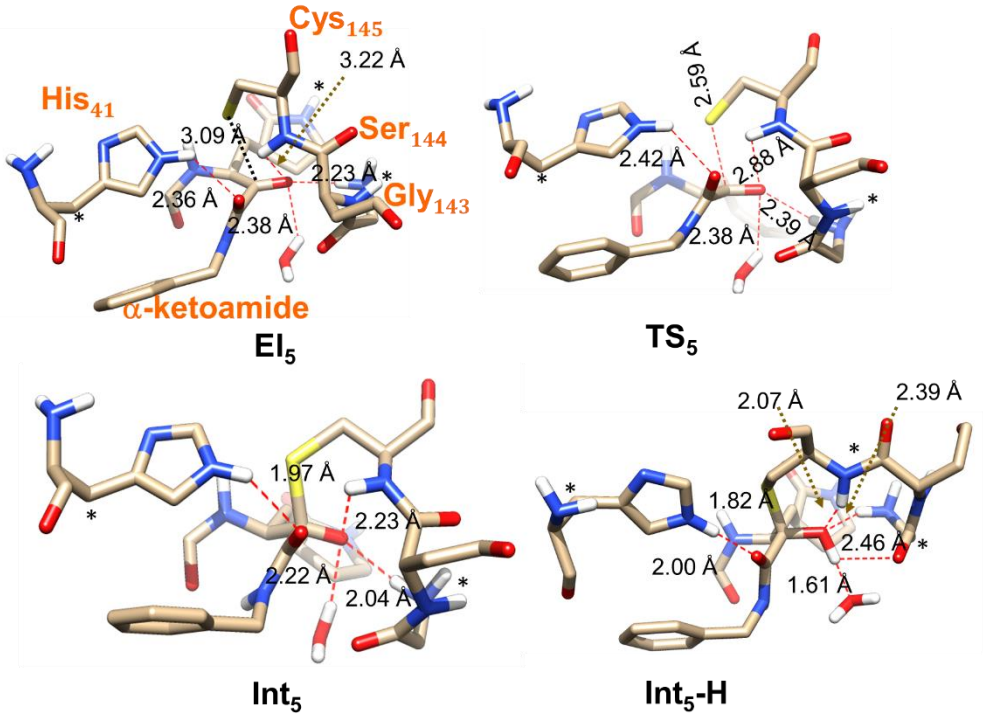

Figure 9. Optimized geometries of the intermediates and transition state of the reaction between M_{pro} and α-ketoamide of the inhibitor from *Re* face. Atoms marked with asterisks are fixed during the geometry optimization. For the sake of clarity, only polar hydrogen atoms are shown.

3.4 The noncovalent interaction and stability of hydroxyl/oxyanion holes of R- and S-thiohemiketal

To explore the noncovalent interactions including H-bonding in oxyanion, we extracted the crystal structure and added hydrogen atoms in the missing position and reoptimized with respect this added hydrogen. To examine the oxyanion, first, we tried to optimize the geometry by deleting the proton on oxyanion, but, in case of S-adduct, all attempt to obtain oxyanion in the presence of His_{41} NεH are failed, resulting in the transfer of a proton from Nε H to O^{-}. However, in this adduct, we notice that the hydroxyl hole is stabilized by four nearby polar atoms, namely, Nε of His_{41}, amide H of warhead, and slightly by H of accessible H_2O (W_1) and another amide H of inhibitor (See Figure 10). The corresponding distances are 1.72, 1.77, 2.96, and 3.00 Å, respectively. Notably, only two of them form hydrogen-bonds with the oxyanion as evident from Bader's QTAIM plot (Figure 10b), and the orientation of non-covalent interaction is such that an 'hydroxyl hole' is formed. We detected two bcps, namely, cp_1 and cp_2,

correspond to two strong H-bonds with the electron densities of 0.0513 and 0.0458 a.u., respectively. Also, we computed the H-bond energy associated with the bcps. To calculate the H-bond energy, we used the following latest formula derived by Emamian *et al.* [50] at the very accurate CCSD(T)/jul-cc-pVTZ level including basis set superposition error (BSSE) bond correction as well as SAPT2+(3)δMP2/aug-cc-pVTZ level, the latter allows the bond energy to be decomposed into physically meaningful components to shed light on the electronic nature of the considered hydrogen bond interactions:

$$\text{Hydrogen bond energy (kcal/mol)} = -223.08 \times \rho_{bcp}\ (\text{a. u.}) + 0.7423 \qquad (3)$$

Furthermore, the amidic oxygen is stabilized by NH of triad residues Cys_{145}–Ser_{144}– Gly_{143}, forming three H-bonds of 2.06, 2.77, and 1.88 Å, respectively. These H-bonds are characterized by three bcps, namely, cp_3, cp_4, and cp_5, and their respective ρ and $\nabla^2\rho$ values are shown in Table 2. The computed H-bond energy of them are −3.60, −2.09, and −6.21 kcal/mol, respectively. Thus, such a huge stability, by the H-bonds, of the α-ketoamide warhead reminds us of the advantage of the α-ketoamide compared to the other inhibitor-warhead.

Figure 10c and d show a scatter plots of RDG S *vs* sign(λ2)ρ and color-filled RDG isosurfaces depicting noncovalent interaction region. Although we obtained several π–π, CH–π, and H-bond interactions from the calculations, we discussed only the interactions related to α-ketoamide motif.

The thiohemiketal of R stereochemistry experiences completely an opposite interacting residues due to the addition of incoming nucleophile from *Re* face. For example, the hydroxyl group at thiohemiketal forms three hydrogen bonds, with the triad residues Cys_{145}–Ser_{144}– Gly_{143} at M_{pro}, of 1.99, 3.09, and 2.52 Å, respectively, and additionally, forms another H-bond with crystallographic water W_1 (Figure 10a). The QTAIM analysis (Table 2) found three are bcps, namely, cp_1, cp_2, and cp_3 correspond to the H-bonds α-keto O–Cys_{145} NH, α-keto O–Gly_{143} NH, and α-keto OH–W_1 O but not with the Ser_{144}

residue. The experimental result also supports this fact.[27] For these H-bonds bonds, the H-bond energy computed according to eqn (3) are –4.79, –1.08, and –5.43 kcal/mol, respectively.

Besides, unlike S-adduct, the amidic oxygen is stabilized by a very strong H-bond with His_{41} NεH of 1.40 Å. The QTAIM result shows that the ρ and $\nabla^2\rho$ values at the bcp (cp_4) are 0.0850 and 0.3334 a.u., respectively. Obviously, the H-bond energy is also high: –18.21 kcal/mol.

Finally, the covalent nature of S–αC bond in both the thiohremiketal, R– and S– stereochemistry, is charecterized from their bcps (cp_5 and cp_6) and their ρ and $\nabla^2\rho$ values. The covalent bond is usually characterized by a negative Laplacian and a negative energy density. Here, for the R-adduct, the energy density and $\nabla^2\rho$ values are –0.1052 and –0.1884 a.u., respectively, while for the S-adduct, the energy density and $\nabla^2\rho$ values are –0.0980 and –0.1718 a.u., respectively.

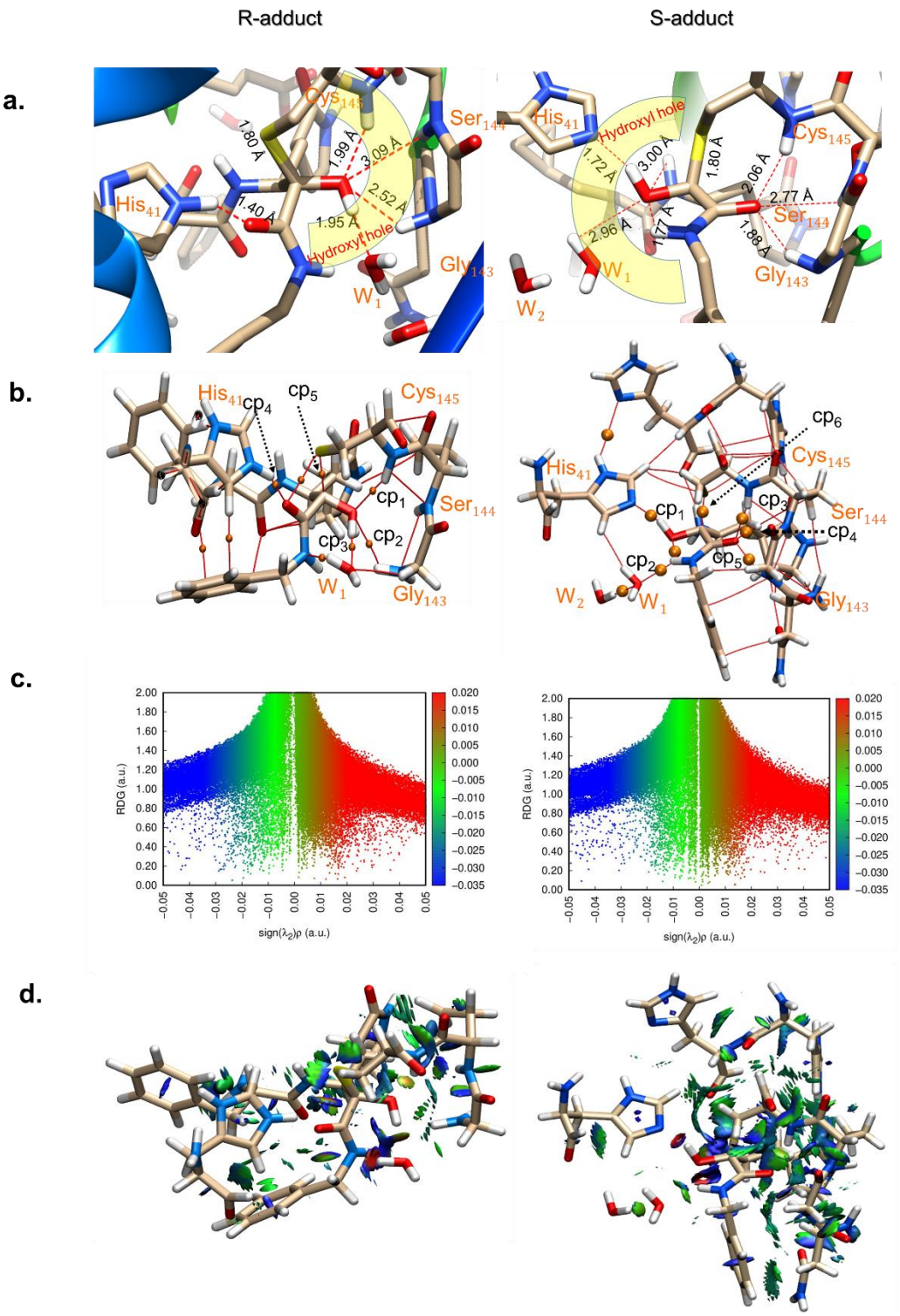

Figure 10 Hydroxyl holes of the R– and S–thiohemiketal of the 5n19 and 6y2f crystal structures, respectively. a) H-bonds between the oxygen atoms of hydroxyl hole and amide moiety in warhead with the hydrogen atoms of coronavirus enzyme residue. b) Some selected QTAIM bond critical points indicating by orange sphere. (See Table 2 for details) c) Scatter plots of reduced density gradient (S) *vs* sign(λ2)ρ. d) Color-filled RDG isosurfaces depicting noncovalent interaction region. The color coding scheme used for isosurfaces is as follows: blue for attractive, red for repulsive, and green for intermediate interactions.

Table 2 The values of electron density ρ and its Laplacian $\nabla^2\rho$ at the important BCPs along with H-bond energy in the interaction between inhibitor-warhead and active enzyme site of the crystal structures of R- and S-thiohemiketal. See Figure 10 for the labelling of BCP.

BCP	Connected atoms	ρ (a.u.)	$\nabla^2\rho$ (a.u.)	H-bond energy (kcal/mol)
R-thiohemiketal				
cp_1	α-keto O–Cys_{145} NH	0.0248	0.0849	–4.79
cp_2	α-keto O–Gly_{143} NH	0.0082	0.0331	–1.08
cp_3	α-keto OH–water O	0.0277	0.0963	–5.43
cp_4	α-ketoamidic O–His_{41} NεH	0.0850	0.3334	–18.21
cp_5	α-keto C–Cys_{145}S	0.1657	–0.1884	–
S-thiohemiketal				
cp_1	α-keto O–His_{41} NεH	0.0513	0.1492	–10.70
cp_2	α-keto O–α-keto amidic N	0.0458	0.1975	–9.47
cp_3	α-ketoamidic O–Cys_{145} NH	0.0195	0.0707	–3.60
cp_4	α-ketoamidic O–Ser_{144} NH	0.0127	0.0495	–2.09
cp_5	α-ketoamidic O–Gly_{143} NH	0.0312	0.1122	–6.21
cp_6	α-keto C–Cys_{145}S	0.1613	-0.1718	–

3. CONCLUSION

In the present paper, we report a theoretical investigation of the reaction mechanism of α-ketoamide based inhibitor with coronavirus main protease M_{pro} by using DFT and semi-empirical quantum mechanical method within ONIOM model. Our calculation was based on the crystal structure of free coronavirus protease (pdb:6y2e) and the coronavirus–inhibitor complexes of both S and R stereochemistry (respectively, pdb:6y2f and pdb:5n19).

We fulfilled main objectives, namely, to characterize of the noncovalent and covalent interactions between the enzyme active site and inhibitor warhead by using NCI-RDG and Bader's QTAIM, and to uncover the mechanism of thiohemiketal formation between cysteine protease and α-ketoamide inhibitor. All the results compared with the experimental data.

Apart from the common two-step pathway *via* $CysS^{-}/His41^{+}$ ion pair formation (pathway 4), we propose three more concerted pathways without forming an ion pair. We have identified and characterized all the stationary points including intermediates and transition states on the PES. Since for the reversible covalent-inhibitor, the change of non-covalent to covalent state is crucial,[40] we identified each state properly by applying AIM and NBO analyses.

The computed kinetic and thermodynamic parameres show that although Pathway 1 has high activation barrier, pathway 2 and 3 have comparable activation barriers with the traditional pathway 4. Also, all these steps are highly exoergic due to the high stability of the oxyanion/hydroxyl hole. Nevertheless, the exoergicity of pathway 3 is slightly less (*ca.* −4.2 kcal/mol) making the ΔE_{act} of the reverse reaction, that is, $\mathbf{Int_3 \rightarrow EI_3}$, low (*ca.* 2.8 kcal/mol). This indicates the reversible binding nature of the inhibitor. Another notable feature, derived from PCM calculation at ε =4, is that for all except *Re* face reaction, the nucleophilic-attacking steps have higher $\Delta_r E$ in the gas phase. This is probably due to greater stabilization of non-covalent enzyme−inhibitor complex (reactant side) than that of covalent S−thiohemiketal complex (product side).

In conclusion, our computed results suggest that in addition to the traditional mechanism (pathway 4) the reaction can also proceed *via* the other plausible paths with similar activation barriers.

In the α-ketoamide, the LUMO is π* in nature and resides on α-keto group to accept a lone-pair of electrons from Cys S. Interestingly, here, the LUMO of S-In contains the π* orbital for accepting nucleophile, while in R-In, the lowest energy π* orbital is located on LUMO+1 for such acceptance.

Finally, we have found that in R–thiohemiketal, the α-keto oxygen in the oxyanion/hydroxyl hole is stabilized by three hydrogen bonds, while for S–thiohemiketal, the α-keto oxygen is stabilized by two H-bonds but slightly stronger than in R–thiohemiketal. As a result, in both adducts, the sulfur forms S–C covalent bond of similar strengths.

Indeed, the application of extensive QM/MM approach by using full enzyme residues may slightly alter the position of potential energy surfaces in some cases; however, we hope that our model is sufficiently accurate for this work.

In the present situation, we believe that our work is providing extremely relevant and useful information for designing new anti-coronavirus drug by using α-ketoamide as an inhibitor.

SUPPORTING INFORMATION

Figures S1-S5 and Tables S1 along the Cartesian coordinates of all the relevant species are presented in Supporting Information.

AUTHOR INFORMATION

Corresponding Author

* S. Banerjee. Email: sbanchem@gmail.com

ORCID

Snehasis Banerjee: 0000-0003-0888-5870

ACKNOWLEDGMENT

We thank professor A. K. Mukherjee and Dr. Swapnadeep for their helpful suggestion. Also, we thank, Monidipa and Adrika for their kind assistance.

Notes

The authors declare no competing financial interest.

REFERENCES

1. Zhang, L.; Lin, D.; Sun, X.; Curth, U.; Drosten, C.; Sauerhering, L; Becker, S.; Rox, K.; Hilgenfeld, R. Crystal structure of SARS-CoV-2 main protease provides a basis for design of improved α-ketoamide inhibitors, *Science,* **2020**, *368*, 409–412.
2. Jin, Z.; Zhao, Y.; Sun, Y. *et al.* Structural basis for the inhibition of SARS-CoV-2 main protease by antineoplastic drug carmofur. *Nat. Struct. Mol. Biol.* **2020**, *27*, 529–532.
3. Wu, F. *et al.* A new coronavirus associated with human respiratory disease in China. *Nature* **2020**, *579*, 265–269.
4. Zhou, P. *et al.* A pneumonia outbreak associated with a new coronavirus of probable bat origin. *Nature* **2020**, ***579***, 270–273.
5. Jin, Z.; Du, X.; Xu, Y. *et al.* Structure of M_{pro} from SARS-CoV-2 and discovery of its inhibitors. *Nature* **2020**, *582*, 289–293.
6. Kneller, D.W.; Phillips, G.; O'Neill, H.M. *et al.* Structural plasticity of SARS-CoV-2 3CL M^{pro} active site cavity revealed by room temperature X-ray crystallography. *Nat. Commun.* **2020**, *11***,** 3202.
7. Bai, C.; Warshel, A. Critical Differences Between the Binding Features of the Spike Proteins of SARS-CoV-2 and SARS-CoV, **2020**, *J. Phys. Chem B* https://doi.org/10.1021/acs.jpcb.0c04317.
8. *In Silico* Exploration of the Molecular Mechanism of Clinically Oriented Drugs for Possibly Inhibiting SARS-CoV-2's Main Protease, *J. Phys. Chem. Lett*. **2020**, *11*, 4413–4420.

9. Wang. H. He, S.; Deng. W.; Zhang, Y.; Li. G.; Sun. J.; Zhao. W.; Guo. Y.; Yin. Z. Li. D. Shang. L. Comprehensive Insights into the Catalytic Mechanism of Middle East Respiratory Syndrome 3C-Like Protease and Severe Acute Respiratory Syndrome 3C-Like Protease, *ACS Catal.* **2020**, *10*, 5871–5890.
10. Gordon, D.E., Jang, G.M., Bouhaddou, M. *et al.* A SARS-CoV-2 protein interaction map reveals targets for drug repurposing. *Nature,* **2020** https://doi.org/10.1038/s41586-020-2286-9.
11. Ehmke, V. *et al.* Tuning and predicting biological affinity: arylnitriles as cysteine protease inhibitors, *Org. Biomol. Chem* **2012,** *10,* 5764–6768
12. Baillie, T.A. Targeted covalent inhibitors for drug design. *Angew. Chem. Int. Ed.* **2016**, *55*, 13408–13421.
13. Johansson, M.H. Reversible Michael additions: Covalent inhibitors and prodrugs. *Mini Rev. Med. Chem.* **2012**, *12*, 1330–1344.
14. Ettari, R.; Cosconati, S.; Amendola, G.; Chouchene, K.; Wagner, A.; Hellmich, U.A.; Ulrich, K.; Krauth-Siegel, R.L.;Wich, P.R. Development of novel peptide-based Michael acceptors targeting rhodesain and falcipain-2 for the treatment of Neglected Tropical Diseases (NTDs). *J. Med. Chem*. **2017**, *60*, 6911–6923.
15. Breuning, A.; Degel, B.; Schulz, F.; Büchold, C.; Stempka, M.; Machon, U.; Gelhaus, C.; Leippe, M.; Leyh, M.; Kisker, C.; *et al.* Michael acceptor based antiplasmodial and antitrypanosomal cysteine protease inhibitors with unusual amino acids. *J. Med. Chem*. **2010**, *53*, 1951–1963.
16. Ettari, R.; Bonaccorso, C.; Micale, N.; Heindl, C.; Schirmeister, T.; Calabro, M.L.; Grasso, S.; Zappala, M. Development of novel peptidomimetics containing a vinyl sulfone moiety as proteasome inhibitors. *ChemMedChem* **2011**, *6*, 1228–1237.
17. Lonsdale, R.; Ward, R. A. Structure-based design of targeted covalent inhibitors *Chem. Soc. Rev.*, **2018**, *47*, 3816–3830

18. De Risi C.; Pollini G. P.; Zanirato V.; Recent Developments in General Methodologies for the Synthesis of α-Ketoamides, *Chem. Rev.* **2016**, *116*, 3241–3305.
19. Stein, M. L.; Cui, H.; Beck, P.; Dubiella, C.; Voss, C.; Krüger, A.; Schmidt, B.; Groll, M. Systematic comparison of peptidic proteasome inhibitors highlights the α-ketoamide electrophile as an auspicious reversible lead motif. *Angew. Chem., Int. Ed*. **2014**, *53*, 1679-1683.
20. Liang, J.; Pitsillou, E.; Karagiannis, C.; Darmawan, K. K. *et al.* Interaction of the prototypical α-ketoamide inhibitor with the SARS-CoV-2 main protease active site in silico: Molecular dynamic simulations highlight the stability of the ligand-protein complex, *Comput. Biol. Chem*., **2020**, *87*, 107292–107299.
21. Townsend P. A.; Grayson M.N.; Density Functional Theory Transition-State Modeling for the Prediction of Ames Mutagenicity in 1,4 Michael Acceptors, *J. Chem. Inf. Model.* **2019**, *59*, 12, 5099–5103.
22. Voss, C.; Scholz, C.; Knorr, S.; Beck, P.; Stein, M. L.; Zall, A.; Kuckelkorn, U.; Kloetzel, P. M.; Groll, M.; Hamacher, K.; Schmidt, B. α-Keto phenylamides as P1'-extended proteasome inhibitors. *ChemMedChem* **2014**, *9*, 2557–2564.
23. Pacifico, S. *et al.* Synthesis and Biological Activity of Peptide α-Ketoamide Derivatives as Proteasome Inhibitors, *ACS Med. Chem. Lett.* **2019**, *10*, 1086–1092.
24. Ovat, A.; Li, Z. Z.; Hampton, C. Y.; Asress, S. A.; Fernandez, F.́M.; Glass, J. D.; Powers, J. C. Peptidyl α-Ketoamides with Nucleobases, Methylpiperazine, and Dimethylaminoalkyl Substituents as Calpain Inhibitors. *J. Med. Chem.* **2010**, *53*, 6326-6336.
25. Chen J-C. *et. al.* Design and Synthesis of α-Ketoamides as Cathepsin S Inhibitors with Potential Applications against Tumor Invasion and Angiogenesis, *J. Med. Chem*. **2010**, *53*, 4545–4549.
26. Ota, E.; Usui, K.; Oonuma, K.; Koshino, H.; Nishiyama, S.; Hirai, Go.; Sodeoka, M., Thienyl-Substituted α-Ketoamide: A Less Hydrophobic Reactive Group for Photo-Affinity Labeling, *ACS Chem. Biol.* **2018**, *13*, 876–880.

27. Zhang, L. *et al.* α-Ketoamides as Broad-Spectrum Inhibitors of Coronavirus and Enterovirus Replication: Structure-Based Design, Synthesis, and Activity Assessment, *J. Med. Chem*. **2020**, *63*, 4562–4578
28. Quesne, M.; Ward, R.; de Visser, S. P. Cysteine protease inhibition by nitrile-based inhibitors: a computational study, *Frontiers in Chemistry*, **2013**, *1*, 39
29. Jasim, M. H.; Rathbone, D. L. Reaction profiling of a set of acrylamide-based human tissue transglutaminase inhibitors, *J. Mol. Graph. Model.* **2018**, *79*, 157–165.
30. Paasche, A.; Schirmeister, T.; Engels B. Benchmark Study for the Cysteine−Histidine Proton Transfer Reaction in a Protein environment: Gas Phase, COSMO, QM/MM Approaches, *J. Chem. Theory Comput.* **2013**, 9, 1765–1777.
31. Paasche, A.; Schiller M., Tanja S.; Engels B. Mechanistic Study of the Reaction of Thiol-Containing Enzymes with α,β-Unsaturated Carbonyl Substrates by Computation and Chemoassays, *ChemMedChem*, **2010**, *5*, 869-880
32. Klein, P *et al.*, Naphthoquinones as Covalent Reversible Inhibitors of Cysteine Proteases—Studies on Inhibition Mechanism and Kinetics, *Molecules*, **2020**, *25*, 2064.
33. Mario P.; Medina F. E.; Ramos M. J.; Russo N.; Fernandes P. A.; Marino, T. How the Destabilization of a Reaction Intermediate Affects Enzymatic Efficiency: The Case of Human Transketolase, *ACS Catal*. **2020**, *10*, 2872–2881.
34. Arafet, K.; Świderek K.; Moliner,V. Computational Study of the Michaelis Complex Formation and the Effect on the Reaction Mechanism of Cruzain Cysteine Protease, *ACS Omega*, **2018**, *3*, 18613-18622.
35. Wei, D. H.; Huang, X. Q.; Liu, J. J.; Tang, M. S.; Zhan, C. G. Reaction Pathway and Free Energy Profile for Papain-Catalyzed Hydrolysis of N-Acetyl-Phe-Gly 4-Nitroanilide. *Biochemistry* **2013**, *52*, 5145– 5154.

36. Świderek K.; Moline V. Revealing the molecular mechanisms of proteolysis of SARS-CoV-2 Mpro by QM/MM computational methods. Chem. Sci., 2020, https://doi.org/10.1039/D0SC02823A

37. Arafet, K.; Ferrer, S.; Moliner, V. Computational Study of the Catalytic Mechanism of the Cruzain Cysteine Protease. *ACS Catal.* **2017**, *7*, 1207– 1215

38. Shokhen, M., Khazanov, N.; Albeck, A. The mechanism of papain inhibition by peptidyl aldehydes. *Proteins*, **2011**, *79*, 975-985

39. Chatterjee, P.; Botello-Smith, W.M; Zhang, Han.; Qian, Li.; Alsamarah, A.; Kent, D.; Lacroix, J. J.; Baudry, M; Luo, Y. Can Relative Binding Free Energy Predict Selectivity of Reversible Covalent Inhibitors? *J. Am. Chem. Soc*. **2017**, *139*, 17945–17952.

40. Becke, A.D. Density-functional thermochemistry. III. The role of exact exchange, *J. Chem. Phys*. **1993**, *98*, 5648.

41. Lee, C.; Yang, W.; Parr R. G. Development of the Colle-Salvetti correlation-energy formula into a functional of the electron density. *Phys. Rev. B* **1988**, *37*, 785.

42. Stewart. J. J. P. Optimization of parameters for semiempirical methods. V. Modification of NDDO approximations and application to 70 elements, *J. Mol. Model.*, **2007,** *13*, 1173-213.

43. Vreven T.; Morokuma, K.; Farkas, Ö.; Schlegel, H. B.; Frisch, M. J. Geometry optimization with QM/MM, ONIOM and other combined methods. I. Microiterations and constraints, *J. Comp. Chem.*, **2003,** *24*, 760-69.

44. Frisch M. J. et al. Gaussian 09, Gaussian, Inc., Wallingford CT, 2016.

45. Miertuš, S.; Scrocco, E.; Tomasi, J. Electrostatic Interaction of a Solute with a Continuum. A Direct Utilization of ab initio Molecular Potentials for the Prevision of Solvent Effects, *Chem. Phys.* **1981**, *55*, 117-29.

46. Simonson, T.; Brooks, C. L. Charge Screening and the Dielectric Constant of Proteins: Insights from Molecular Dynamics. *J. Am. Chem. Soc*. **1996**, *118*, 8452−8458.

47. Laskowski R A, Swindells M B (2011). LigPlot+: multiple ligand-protein interaction diagrams for drug discovery. *J. Chem. Inf. Model.*, **51**, 2778−2786.
48. Reed, A.E.; Curtiss, L.A.; Weinhold, F. Intermolecular interactions from a natural bond orbital, donor-acceptor viewpoint, *Chem. Rev*. **1988***, 88,* 899−926.
49. Anandakrishnan R.; Aguilar B.; Onufriev. V. A. H++ 3.0: automating pK prediction and the preparation of biomolecular structures for atomistic molecular modeling and simulation, *Nucleic Acids Res*., **2012**, *40*, W537-541.
50. Emamian, S.; Lu T.; Kruse, H.; Emamian, H. Exploring Nature and Predicting Strength of Hydrogen Bonds: A Correlation Analysis Between Atoms-in-Molecules Descriptors, Binding Energies, and Energy Components of Symmetry-Adapted Perturbation Theory, *J. Comput. Chem.*, **2019**, *40,* 2868−2881.

Graphical Abstract

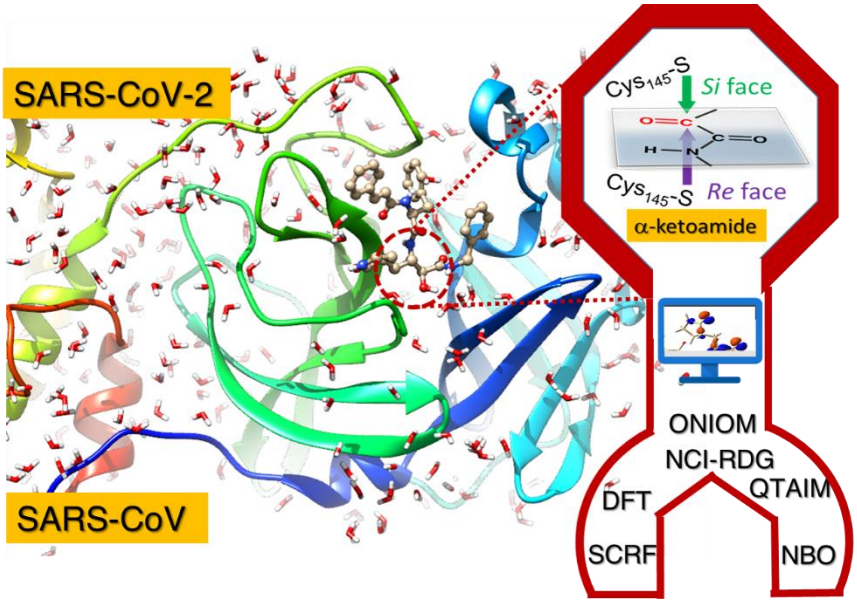
SARS-CoV-2
SARS-CoV
Cys145-S
Si face
Re face
α-ketoamide
ONIOM
NCI-RDG
QTAIM
DFT
SCRF
NBO

Supporting Information

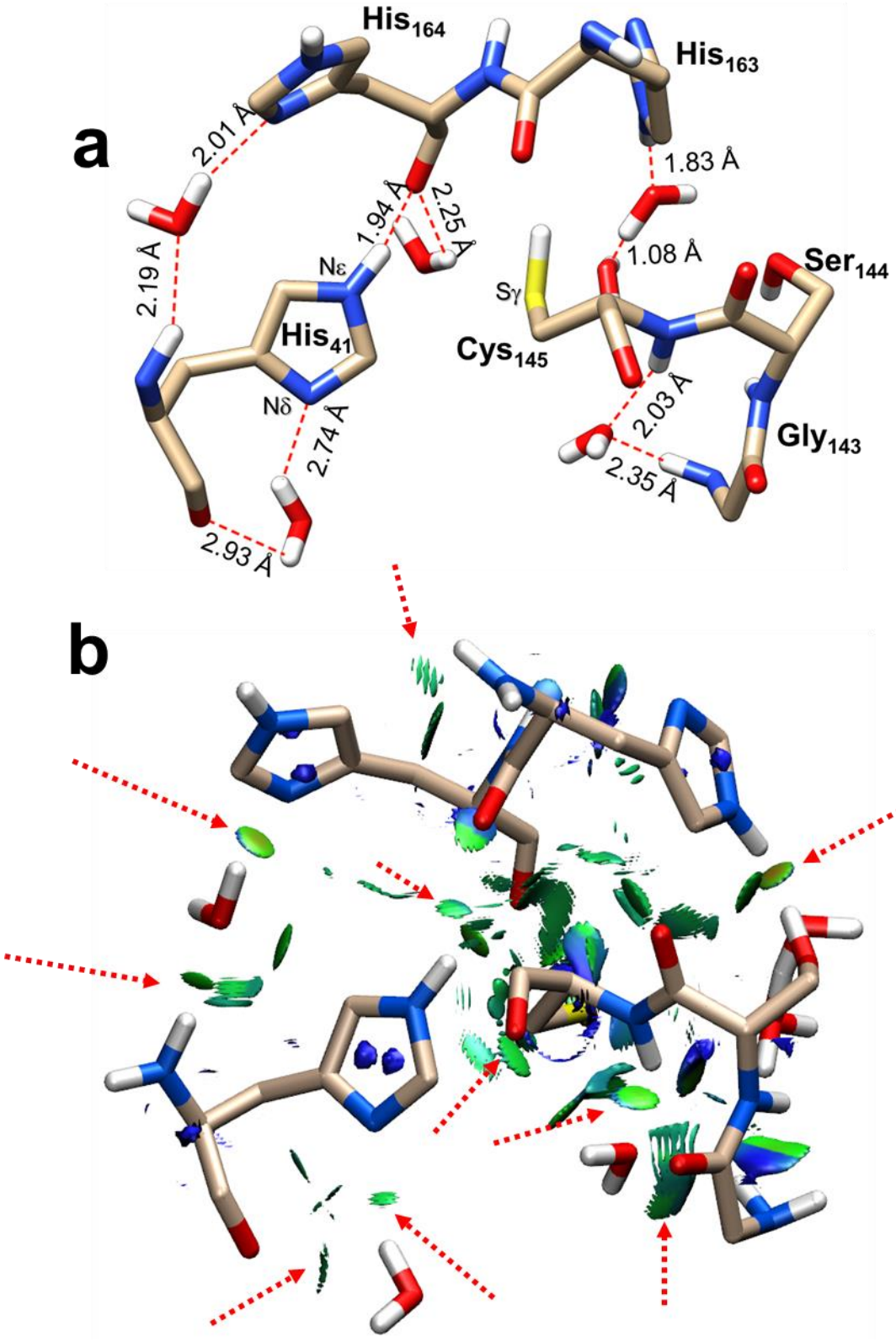
a
His164
His163
2.01 Å
1.83 Å
1.94 Å
2.25 Å
1.08 Å
Ser144
2.19 Å
Nε
Sγ
His41
Cys145
Nδ
2.03 Å
Gly143
2.74 Å
2.35 Å
2.93 Å
b

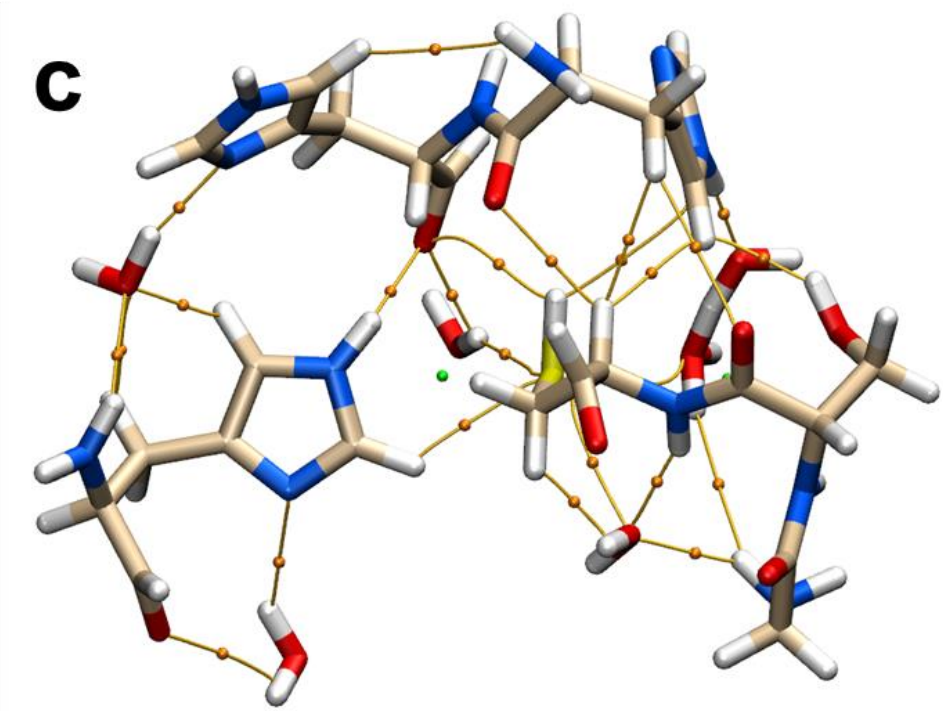

Figure S1 Intermolecular interactions and H-bonds within inhibitor-free enzyme in the active sites with five residues His_{41}, Gly_{143}, Ser_{144}, Cys_{145}, His_{164}, His_{165}, and five crystalline waters a) inter-residual H-bonds b) NCI-RDG isosurface plot; some selected interactions are indicated by red arrow c) QTAIM analyzed bcp (orange sphere) and ccp (green sphere).

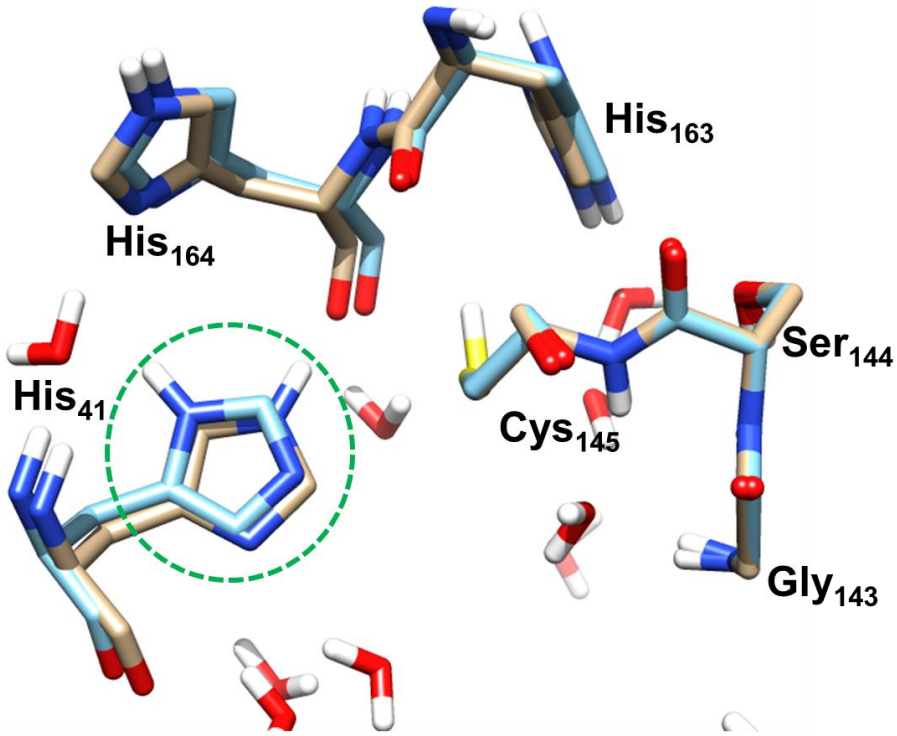

Figure S2 Comparison of structure of enzyme active site in presence (C=khaki) and absence (C= Cyan) of inhibitor. The green circle indicates the rotation of imidazole ring of His_{41}.

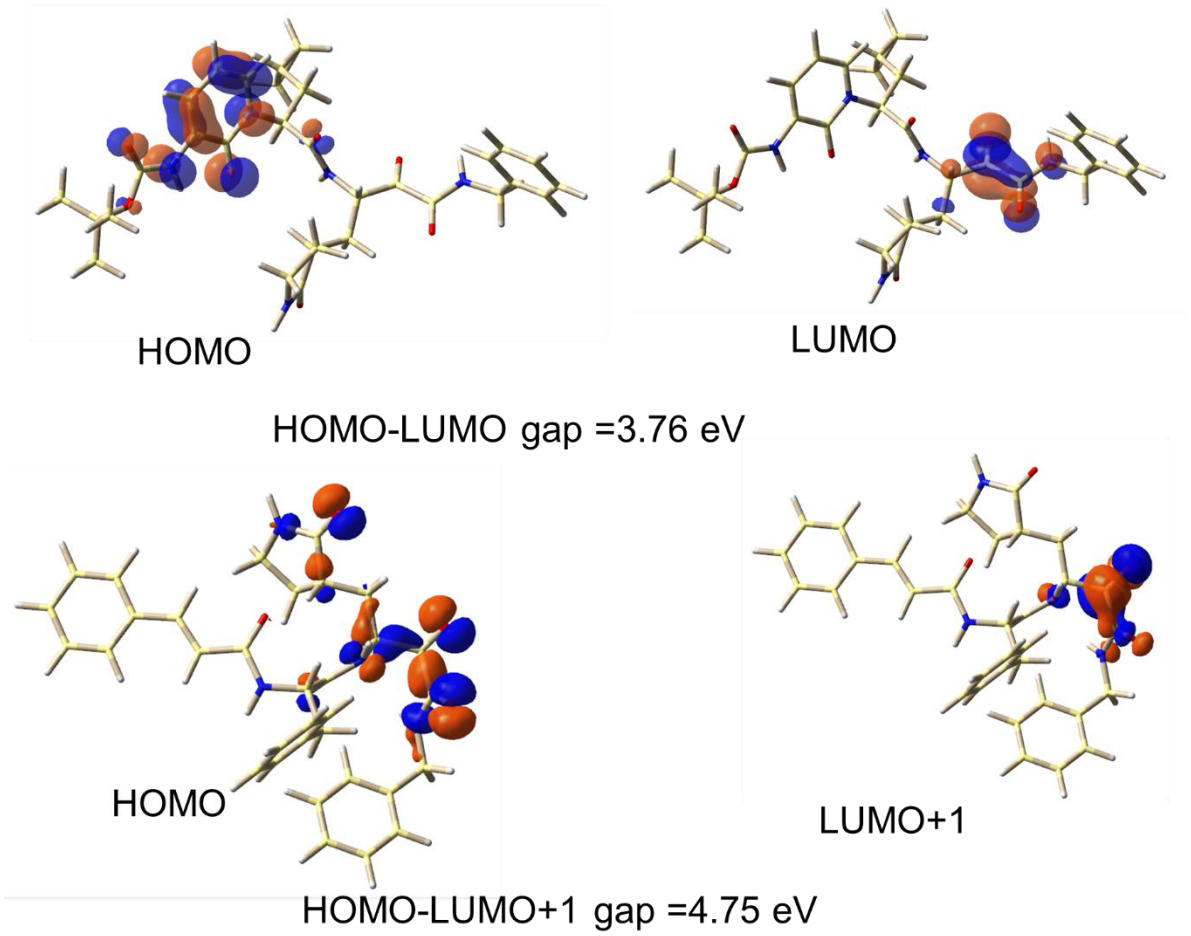

Figure S3 Frontier Molecular Orbitals of the investigated inhibitor optimized at B3LYP/631G(d) level

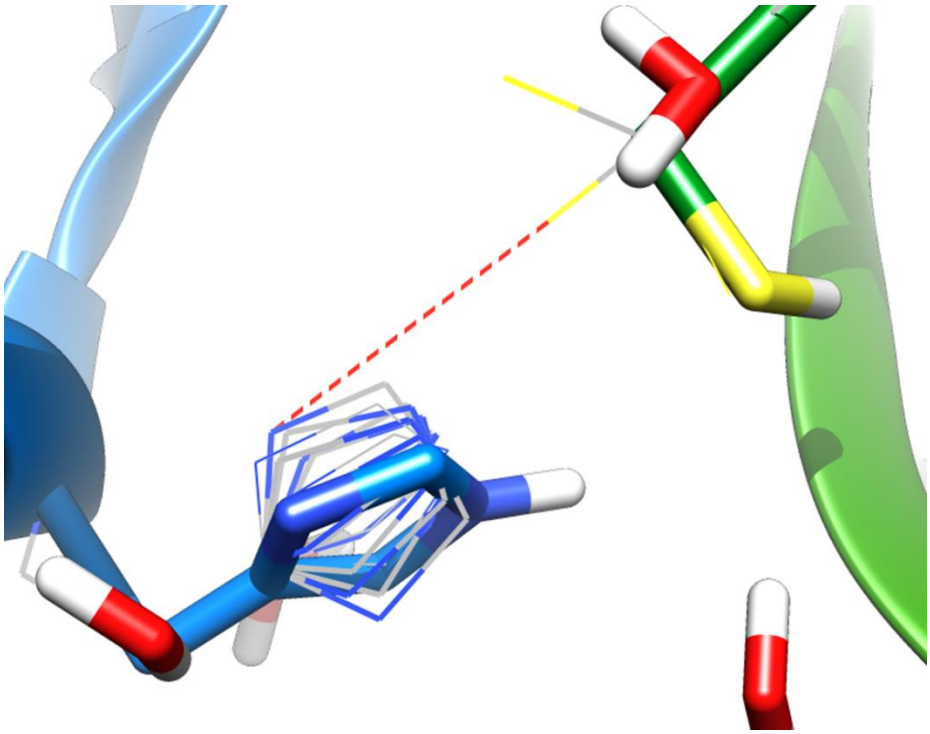

Figure S4 Rotamers of His_{41} and Cys_{145} in inhibitor free enzyme (Ref. *Structure* **2011**, *19*, 844–858.)

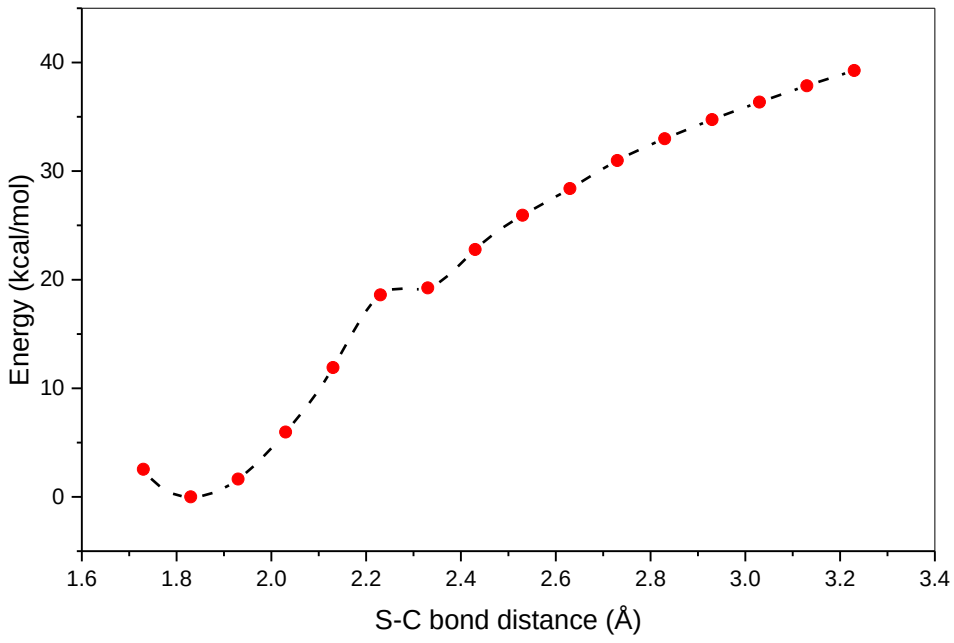

Figure S5 PES scan of S–αC distances the second step reaction pathway 4.

Table S1 NBO second order perturbation theory analysis for the transition states involved in the investigated species

	Donor (i)→Acceptor(j)	E^2 (kcal/mol)
TS1	$n_{O(\alpha C)} \rightarrow \sigma^*_{S-H}$	165.1
	$n_{O(\alpha C)} \rightarrow \sigma^*_{N\varepsilon-H}$	15.5
TS2	$n_S \rightarrow \sigma^*_{\alpha C=O}$	11.5
	$n_S \rightarrow \sigma^*_{O-H(W)}$	199.5
	$n_{O(\alpha C)} \rightarrow \sigma^*_{O-H(W)}$	83.4
TS3	$n_S \rightarrow \sigma^*_{O-H(W1)}$	139.6
	$n_{O(W1)} \rightarrow \sigma^*_{O-H(W2)}$	127.2
	$n_{N\delta} \rightarrow \sigma^*_{O-H(W2)}$	66.3
	$n_S \rightarrow \sigma^*_{\alpha C-O}$	15.0
TS3_pt	$n_{N\delta} \rightarrow \sigma^*_{O-H}$	230.1
TS3_ptw	$n_{O(W3)} \rightarrow \sigma^*_{N\varepsilon-H}$	149.6
	$n_{O(\alpha C)} \rightarrow \sigma^*_{O-H(W3)}$	263.1
TSZ	$n_S \rightarrow \sigma^*_{O-H}$	200.5
	$n_{N\delta} \rightarrow \sigma^*_{O-H}$	240.1
TS4	$n_S \rightarrow \sigma^*_{\alpha C-O}$	5.1
	$n_{N\varepsilon} \rightarrow \sigma^*_{O-H}$	55.2
TS5	$n_S \rightarrow \pi^*_{\alpha C-O}$	22.89
	$n_{O(\alpha C)} \rightarrow \sigma^*_{N-H(Gly143)}$	8.2
	$n_{O(amidic)} \rightarrow \pi^*_{N-H(cys145)}$	16.8